Topological Phases of Sound and Light

V. Peano,[1] C. Brendel,[1] M. Schmidt,[1] and F. Marquardt[1,2]
[1]Institute for Theoretical Physics, Friedrich-Alexander-Universität Erlangen-Nürnberg, Staudtstraße 7, 91058 Erlangen, Germany
[2]Max Planck Institute for the Science of Light, Günther-Scharowsky-Straße 1, 91058 Erlangen, Germany
(Received 6 February 2015; published 28 July 2015)

Topological states of matter are particularly robust, since they exploit global features of a material's band structure. Topological states have already been observed for electrons, atoms, and photons. It is an outstanding challenge to create a Chern insulator of sound waves in the solid state. In this work, we propose an implementation based on cavity optomechanics in a photonic crystal. The topological properties of the sound waves can be wholly tuned *in situ* by adjusting the amplitude and frequency of a driving laser that controls the optomechanical interaction between light and sound. The resulting chiral, topologically protected phonon transport can be probed completely optically. Moreover, we identify a regime of strong mixing between photon and phonon excitations, which gives rise to a large set of different topological phases and offers an example of a Chern insulator produced from the interaction between two physically distinct particle species, photons and phonons.

DOI: 10.1103/PhysRevX.5.031011

Subject Areas: Nanophysics, Photonics, Topological Insulators

I. INTRODUCTION

Recently, a new paradigm in the classification of the phases of matter has emerged that is based on topology [1]. The Hall conductance quantization in a 2D electron gas placed inside a magnetic field is so precise that it serves as a standard to define the Planck constant. The precision is due to the current being carried by chiral edge states which are robust against scattering by disorder. It was realized that at the heart of this effect there is the nontrivial topology of the bulk electron band structure encoded in topological invariants, the Chern numbers [2]. The modern exploration of new topological phases started with the prediction of the anomalous quantum Hall effect [3]. This is a so-called Chern-insulator state that is realized in a staggered magnetic field that has a vanishing average. The subsequent discovery of the quantum spin Hall effect [4,5] then proved that even time-reversal symmetry breaking is not necessary. In this case, the nontrivial topology is induced by the spin-orbit coupling. A third pathway to a nontrivial topology is the time-dependent modulation of the band structure in Floquet topological insulators [6–9].

Inspired by these new developments in our understanding of electronic systems, researchers have begun to extend the concept to other settings. Proposals and first experiments on topological phases exist for cold atoms and ions (see, e.g., Refs. [10–14]). More closely related to our setting is the theoretical [15–21] as well as experimental [9,22–25] investigation of topologically nontrivial phases of light (see Ref. [26] for a recent review). Unlike electrons, photons are electrically neutral. Nevertheless, they mimic the dynamics of charged particles while hopping on a lattice, e.g., when the time-reversal symmetry is broken by synthetic gauge fields [15,16,18–20] or when an effective spin-orbit coupling is engineered [17,21,23].

At present, it remains an outstanding challenge to engineer topological phases for sound waves (phonons) in the solid state, with the resulting robust chiral edge state transport that is useful for applications in phononics. So far, topological properties have been conjectured to be present in the vibrations of individual microtubule macromolecules in biophysics [27], although the precise mechanism requires further investigation. Moreover, recently it was pointed out that masses connected by springs or rigid links in special networks (related to isostatic lattices) show topological features of vibrations. These include zero modes localized at some sample edges of an appropriate geometry [28], propagation of topologically protected nonlinear solitary waves [29] in 1D chains, and topologically robust defect modes bound to dislocations inside a 2D lattice [30]. In contrast to those works, here we propose a 2D phonon metamaterial of the Chern-insulator class that shows chirally propagating edge states robust against disorder. Very recently, there have been steps in this direction for macroscopic systems, employing circulating fluid currents [31] to break time-reversal invariance, or wiring up pendula [32] in the appropriate way to create a

topological insulator. Our goal is to propose a fully tunable nanoscale system.

It is not trivial to engineer the required nonreciprocal phases for the transport of phonons in a tunable solid-state platform. Although it would be conceivable to employ local time-dependent modulation of the stress, e.g., using electrodes and piezoelectric materials (essentially emulating the route towards photonic magnetic fields proposed in Ref. [19]), this is not very practical, since the number of wires would scale with the system size.

The tool we employ instead is cavity optomechanics [33], a rapidly evolving field that studies the interaction between radiation and nanomechanical motion, with possible applications in sensing, classical and quantum communication, and tests of foundational questions in quantum physics. In particular, we consider the flexible and scalable platform of optomechanical (OM) crystals [34–38]. These systems are based on freestanding photonic crystals, where engineered defects support colocalized optical and vibrational modes interacting via radiation pressure. Recently, it has been proposed that an array of such point defects would form an optomechanical array "metamaterial" where the resulting optical and mechanical band structures could be tuned *in situ* by a driving laser [39]. Here, we show how to implement a nontrivial topology for sound waves in a solid-state device, based on such optomechanical arrays. This can be achieved when a suitable lattice geometry is chosen and the driving laser imprints an appropriate phase pattern on the optomechanical interaction. The light field then induces an effective Hamiltonian for the sound waves that leads to a Chern insulator with robust edge modes. We emphasize that a single laser field (with a suitable phase pattern) is enough; no time-dependent modulation of any kind is required in our approach. Our proposal not only presents a practicable route towards phonon Chern insulators in the solid state, but its realization would also represent the first example of a topological state of matter produced using optomechanics.

In addition, we find that upon sweeping the laser frequency one can also enter a regime where it is no longer possible to view phonons and photons as separate. Instead, a whole series of topological phase transitions arises where both sound and light are involved. This would be an example of a topologically nontrivial hybrid band structure made of two physically distinct particle species, with corresponding edge states for the emerging hybrid excitations. In contrast to the recently proposed photon-exciton topological polaritons [40–42], the interaction in our case is tunable *in situ* over a wide range via the laser amplitude.

II. RESULTS

A. Optomechanical arrays

In the field of cavity optomechanics [33] the basic interaction between light and mechanical motion comes about because any deformation of an optical cavity's boundaries will lead to a shift of the cavity's optical mode frequencies. Focusing on a single cavity mode, its energy may therefore be expressed as $\hbar\omega_{\mathrm{cav}}(\hat{x})\hat{a}^\dagger\hat{a}$, where $\hat{x}$ represents the mechanical displacement and $\hat{a}^\dagger\hat{a}$ is the photon number. Expanding to leading order in $\hat{x}$, which is usually an excellent approximation [33], this yields the basic interaction $\hbar\omega'_{\mathrm{cav}}\hat{x}\hat{a}^\dagger\hat{a}$. The mechanical motion is very often dominated by a single harmonic vibration mode, such that $\hat{x} = x_{\mathrm{ZPF}}(\hat{b} + \hat{b}^\dagger)$, with x_{ZPF} the mechanical zero-point fluctuations and $\hat{b}$ the phonon annihilation operator. Thus, one arrives at the fundamental optomechanical interaction

$$-\hbar g_0 \hat{a}^\dagger\hat{a}(\hat{b} + \hat{b}^\dagger), \tag{1}$$

where $g_0 = -\omega'_{\mathrm{cav}}x_{\mathrm{ZPF}}$ is the bare coupling constant. The optomechanical coupling rate g_0 represents the optical shift due to a mechanical zero-point displacement, and it is typically much smaller than the photon decay rate κ. However, by illuminating the sample with laser light, one can effectively enhance the optomechanical interaction. When the system is driven by a laser, one can write $\hat{a} = \alpha + \delta\hat{a}$, where α is the complex amplitude set by the laser drive and $\delta\hat{a}$ represents the quantum fluctuations on top of that. Keeping the leading nontrivial terms, one obtains a quadratic Hamiltonian (the so-called linearized optomechanical interaction),

$$-\hbar g_0(\alpha^*\delta\hat{a} + \alpha\delta\hat{a}^\dagger)(\hat{b} + \hat{b}^\dagger). \tag{2}$$

This is the well-tested basis for the description of almost all quantum-optomechanical experiments to date [33]. The new, effective coupling constant $g = g_0\alpha$ is laser tunable and may be complex, containing a phase factor set by the laser phase, which becomes crucial in our scheme. Equation (2) describes the interconversion between phonons and photon excitations at the cavity mode frequency (terms $\delta\hat{a}^\dagger\hat{b}$ and $\delta\hat{a}\hat{b}^\dagger$). Physically, these conversion processes can be understood as anti-Stokes Raman transitions, where the driving photons impinging on the cavity are inelastically scattered into higher-frequency photons by absorbing a phonon (enabling, e.g., laser cooling of mechanical motion). Depending on the laser frequency, there can also be Stokes processes, where driving photons are scattered to lower frequencies while creating a phonon ($\delta\hat{a}^\dagger\hat{b}^\dagger$), although these are not important for our scheme. For notational simplicity (and following convention), from now on we replace $\delta\hat{a}$ by $\hat{a}$.

In the solid state, the largest values of g_0 have been reached in OM crystals [34–38]. These are freestanding photonic crystals, i.e., dielectric slabs with an appropriate pattern of holes that creates complete optical and mechanical band gaps. A local modification of the pattern of holes generates a point defect where optical and mechanical

modes can become localized. The OM interaction between such a localized optical and mechanical mode is described by Eq. (1), with g_0 on the order of around 1 MHz.

Future optomechanical arrays [43–46] can be produced by fabricating a periodic array of such point defects, in 1D or 2D. The localized modes on adjacent lattice sites will have an evanescent overlap, leading to tunneling of photons and phonons between sites i and j with rates J_{ij} and K_{ij}, respectively [43,46,47]. For photons, such tunneling-induced transport between localized modes has been demonstrated experimentally in photonic crystal coupled resonator waveguide arrays [48].

Combining both the optomechanical interaction at each site j as well as the tunneling between sites, the generic optomechanical array Hamiltonian [46,49] reads

$$\hat{H}/\hbar = \sum_j \Omega \hat{b}_j^\dagger \hat{b}_j - \Delta \hat{a}_j^\dagger \hat{a}_j - (g_j \hat{a}_j^\dagger \hat{b}_j + \text{H.c.}) + \hat{H}_{\text{hop}}. \quad (3)$$

The annihilation operators of photons and phonons are denoted by $\hat{a}_j$ and $\hat{b}_j$, where the site index $j = (j_1, j_2, s)$ will include a sublattice label s for a non-Bravais lattice. The $\hat{a}_j$ are already displaced by the classical steady-state light amplitude α_j, set by the laser amplitude (as explained above), and the $\hat{b}_j$ are displaced by the static mechanical displacement β_j, set by the constant radiation force; see Appendix A. The term $\hat{H}_{\text{hop}}/\hbar = -\sum_{i,j} J_{ij} \hat{a}_i^\dagger \hat{a}_j - \sum_{i,j} K_{ij} \hat{b}_i^\dagger \hat{b}_j$ incorporates the hopping of photons and phonons between different sites, and Δ is the laser detuning from the optical resonance, $\Delta \equiv \omega_L - \omega_{\text{cav}}$, as we switched to a frame rotating at the laser frequency. To be clear, we note that the detuning Δ defined here already includes a static effective shift of the optical resonance due to the mechanical displacement β_j, which depends on the laser intensity and is found from the self-consistent classical solution. This is already known well for the standard optomechanical system [33].

The optomechanical interaction displayed in Eq. (3) converts phonons into photons propagating inside the array (and vice versa). The strength of these processes is described by a laser-tunable coupling constant $g_j = g_0 \alpha_j$ that is parametrically enhanced by the light amplitude, where $|\alpha_j|^2$ would be the steady-state photon number in mode j. The amplitude α_j depends on the site j for the case of an inhomogeneous driving field, which we consider below. For the sake of simplicity, we omit the Stokes transitions of the type $\hat{a}_j^\dagger \hat{b}_j^\dagger$, where photon-phonon pairs are emitted (or annihilated). Stokes processes are strongly suppressed in the parameter regime that will turn out to be suitable for the topologically nontrivial phase (where Δ will be negative, corresponding to a "red-detuned" laser drive), so we neglect them at first. Since the anti-Stokes processes considered here conserve the total excitation number, Hamiltonian Eq. (3) is equivalent to a single-particle Hamiltonian, and we are able to use the standard classification of topological phases [1].

B. Chern insulator implemented in an optomechanical array

In multimode OM systems, the optical backaction can be used to engineer the effective mechanical interaction, which has been suggested to pave the way to phononic quantum information processing (see, e.g., Refs. [50,51]). In this context, the phonon hopping amplitudes are modified by the new pathways that are opened by the OM interaction. A phononic excitation can be virtually converted into a photon on site i, hop to site j, and be converted back into a phonon on site j. From standard perturbation theory, the probability amplitude associated with this pathway is $J_{ij} g_i g_j^* / (\Omega + \Delta)^2$. Hence, a pattern of phases in the optomechanical coupling g_j can lead to a synthetic gauge field for phonons in the form of effective hopping rates $K_{ij}^{(\text{eff})} = K_{ij} + K_{ij}^{(\text{opt})}$ that contain an optically induced component with complex phases [51].

Inspired by previous studies that have indicated that a staggered magnetic field for particles on a kagome lattice yields topologically nontrivial phases [16,52–54], our investigations focus on a kagome optomechanical array. We choose this geometry since it can be naturally implemented in 2D optomechanical crystals based on the snowflake design [47,55], which have been demonstrated in an experiment recently [38]. The general approach described here is of course applicable to other lattice geometries as well. The kagome optomechanical array is sketched in Fig. 1. The idea is to have hexagonal patches of periodically arranged snowflake-shaped holes, with linear dislocation defects forming at the edges between those patches. As has been shown in the experiment [38], a suitable modification of the hole pattern inside the linear defect then creates a pointlike defect with localized modes. The nearest-neighbor coupling between those modes will generate the connectivity of a kagome lattice. Its unit cell contains three sites ($s = A, B, C$) forming an equilateral triangle (we set the side to 1). Thus, the optomechanical band structure will comprise altogether six bands, three of them photonlike and three phononlike.

Some general properties of the band structure can be deduced purely from the symmetry of the kagome lattice geometry, without assuming anything about the range of the hopping or other details. The hopping term $\hat{H}_{\text{hop}}$ maintains the time reversal $\mathcal{T}$, the inversion symmetry $\mathcal{I}$ with respect to any corner of the triangle, and the symmetry $\mathcal{C}_3$ (rotations by $n2\pi/3$ around the triangle center, $n \in \mathbb{Z}$). Then, in the absence of the laser drive there is no optical or mechanical band gap: For both the photons and the phonons, the central band touches one of the remaining bands (top or bottom) at the center of the Brillouin zone, $\vec{\Gamma} = (0, 0)$, and the other one at the symmetry points, $\vec{K} = (2\pi/3, 0)$ and $\vec{K}' = (\pi/3, \pi/\sqrt{3})$, where Dirac cones form.

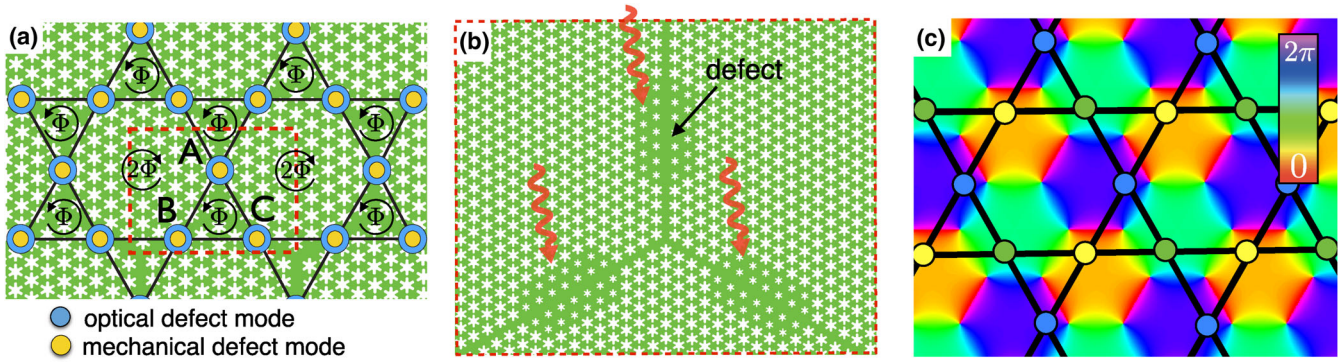

FIG. 1. A kagome optomechanical array. (a) Sketch of the overall arrangement of optical and vibrational modes, with nearest-neighbor hopping on a kagome lattice. The effective magnetic fluxes (indicated) add up to zero, realizing a Chern insulator. (b) Schematic representation of the elementary building block in a possible realization based on a 2D snowflake optomechanical crystal [for clarity, the snowflake size in (a) had been exaggerated in comparison]. The picture shows three linear defects that form at the interfaces between hexagonal domains of a periodic snowflake hole pattern. In the center of each, there is an engineered localized pointlike defect mode (as in the experiment of Ref. [38]). (c) Suitable optical phase pattern, generated by the superposition of three beams meeting at 120° angles in the plane of the sample (illustrated here for a scalar field).

We now assume the lattice to be driven by a laser, with an optical phase that depends on the site within the unit cell, leading to $g_j = ge^{i\varphi_s}$. To retain the $\mathcal{C}_3$ symmetry, we choose a phase mismatch of $2\pi/3$ between the sublattices, $\varphi_B - \varphi_A = \varphi_C - \varphi_B = \varphi_A - \varphi_C = 2\pi/3$. Physically, the driving laser phase pattern has to form a vortex around each triangle center (Fig. 1). This can be achieved via wave front engineering of the impinging laser field. As opposed to our recently proposed optomechanical generation of arbitrary synthetic magnetic fields for photons [39], we emphasize that here (i.e., for a Chern insulator of sound waves) only a single laser frequency is needed and that the imprinted optical phase field is periodic in space, greatly simplifying its generation. In fact, one does not even need the versatility of a spatial light modulator for this task. Superimposing three plane waves impinging on the sample automatically creates the required pattern of optical phases, if they are at 120° angles with respect to each other within the plane of the sample. This is illustrated in Fig. 1(c) for the slightly simplified case of three interfering plane waves of a scalar field, and we confirm that it also works when taking into account the vector nature of the electromagnetic field.

C. Band structure and topological classification

The resulting band structure in the presence of such a drive is shown in Fig. 2, and we explain it in more detail below. The site-dependent optomechanical interaction breaks the time-reversal symmetry, thereby opening large gaps between the mechanical bands. As we show, these gaps are topologically nontrivial and lead to topologically protected sound waves propagating at the edge of a finite system.

As discussed before, Hamiltonian Eq. (3) can be translated from its second-quantized form into a single-particle version, where the nature of the excitation (photon versus phonon) is treated as an internal state. Translational invariance permits us to rewrite it in momentum space, using a plane wave ansatz:

$$\hat{H}(\vec{k})/\hbar = \bar{\omega} - \delta\omega\hat{\sigma}_z/2 - (\bar{t} + \delta t\hat{\sigma}_z/2)\hat{\tau}(\vec{k}) - g(\hat{\mu}\hat{\sigma}_x + \hat{\nu}\hat{\sigma}_y). \tag{4}$$

Here, we assume that only nearest-neighbor sites are coupled, although that (reasonable) approximation could be lifted without destroying any of the essential physical properties discussed in the following; see Appendix B. The binary degree of freedom expressed by $\sigma_z = \pm 1$ denotes photon $(+1)$ versus phonon (-1) excitations, and $\hat{\sigma}_{x,y,z}$ are the Pauli matrices in this subspace. Furthermore, we introduce the parameters $\bar{\omega} = (\Omega - \Delta)/2$, $\delta\omega = \Omega + \Delta$, $\bar{t} = (J + K)/2$, and $\delta t = (J - K)$.

The 3×3 matrices $\hat{\mu}$, $\hat{\nu}$, and $\hat{\tau}(\vec{k})$ in Eq. (4) act on the sublattice degree of freedom, referring to the three sites $s = A, B, C$ of the unit cell. The Hermitian hopping matrix $\hat{\tau}(\vec{k})$ encodes motion on the kagome lattice, with $\tau_{AB} = 1 + e^{-i\vec{k}\vec{a}_1}$, $\tau_{AC} = 1 + e^{i\vec{k}\vec{a}_3}$, and $\tau_{BC} = 1 + e^{-i\vec{k}\vec{a}_2}$, where $\vec{a}_1 = (-1, -\sqrt{3})$, $\vec{a}_2 = (2, 0)$, $\vec{a}_3 = (-1, \sqrt{3})$ are the lattice basis vectors. At the symmetry points in the Brillouin zone, the eigenbasis of the $\mathcal{C}_3$ rotations diagonalizes $\hat{\tau}(\vec{k})$: the eigenvectors are the vortex $|\circlearrowleft\rangle \equiv |1, e^{i2\pi/3}, e^{-i2\pi/3}\rangle/\sqrt{3}$, the antivortex $|\circlearrowright\rangle \equiv |1, e^{-i2\pi/3}, e^{i2\pi/3}\rangle/\sqrt{3}$, and the vortex-free state $|\oslash\rangle \equiv |1, 1, 1\rangle/\sqrt{3}$. The matrices $\hat{\mu}$, $\hat{\nu}$ describe the conversion between photons and phonons. When the OM interaction converts a phonon into an array photon, a driving photon is absorbed and its angular momentum is transferred to the array photon. For example, a vortex-free phonon $|M, \oslash\rangle$ is converted into a photon with a vortex, $|O, \circlearrowleft\rangle$ (M, mechanical; O, optical). The remaining allowed transitions

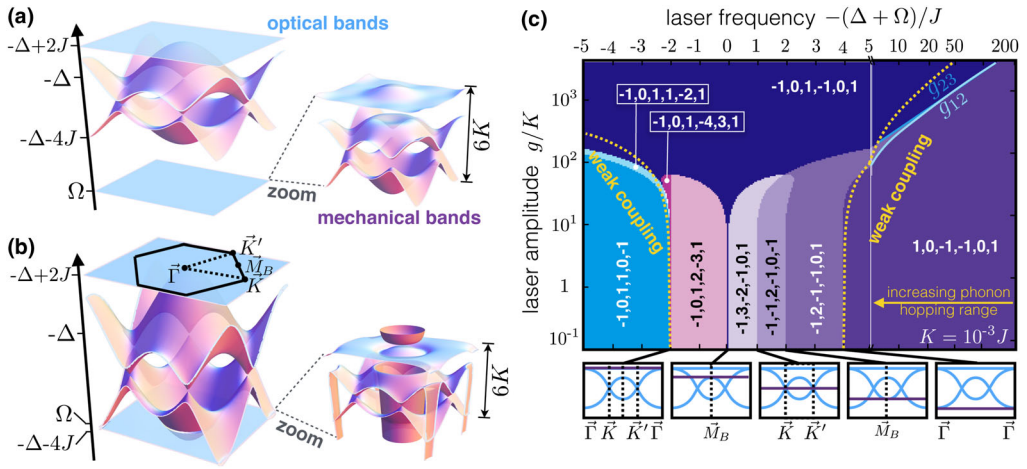

FIG. 2. (a) Band structure of a kagome optomechanical array, shown here in the case of well-separated optical and mechanical bands ("weak-coupling limit"). The three mechanical bands appear flat on the scale of the optical bands. A zoom-in shows the resulting phonon insulator. (b) The "strong-coupling" limit where photon and phonon excitations mix. (c) Topological phase diagram. The different topological phases are marked by the color code and by the set of six Chern numbers, corresponding to the bands ordered by frequency, uniquely identifying each phase. The schematic band structures below the phase diagram indicate the symmetry points where a pair of bands touch at the corresponding phase transition. The OM coupling g (set by the driving laser amplitude) is displayed on a logarithmic scale. The scale of the laser frequency (expressed via the detuning Δ) is linear but switches to logarithmic for large negative detunings, for clarity. The onset of weak coupling is indicated by the line $g = 0.1\Delta_{34}$, where Δ_{34} is the gap between optical and mechanical bands. The approximate analytical expressions (see Appendix D) for the boundaries g_{12} and g_{23} of the intermediate topological phase introduced by the long-range hopping are also shown.

are $|M,\circlearrowleft\rangle \leftrightarrow |O,\circlearrowright\rangle$ and $|M,\circlearrowright\rangle \leftrightarrow |O,\oslash\rangle$. All allowed transitions have matrix element $-g$, and this fully specifies $\hat{\mu}$ and $\hat{\nu}$ in the $\mathcal{C}_3$ eigenbasis (see also Appendix B).

The eigenfrequencies of Hamiltonian Eq. (4) form six photon-phonon polariton bands. The admixture between photon and phonon bands is weak for all quasimomenta if the highest mechanical and lowest optical bands are separated by a gap larger than the OM coupling, $\Delta_{34} \equiv -\Delta - 4J - \Omega + 2K \gg g$, which we call the "weak-coupling limit." Then, the photons can be adiabatically eliminated, arriving at an effective description for the phonons that incorporates the optical backaction.

In the limit of both weak coupling ($\Delta_{34} \gg g$) and large detuning, $\Delta_{34} \gg J$, the optically induced effective phonon hopping $K_{ij}^{(\mathrm{eff})}$ will be restricted to nearest neighbors, whence we arrive at the model investigated in Ref. [16,52,53]. A phonon hopping three times anticlockwise around a triangle, at each step with probability amplitude $K_{ij}^{(\mathrm{eff})} \approx K + e^{-i2\pi/3} Jg^2/(\Delta+\Omega)^2 \equiv K^{(\mathrm{eff})} e^{i\Phi/3}$, picks up the phase (see Appendix C)

$$\Phi = -\frac{3\pi}{2} + 3\arctan\frac{2K(\Delta+\Omega)^2 - Jg^2}{\sqrt{3}Jg^2}. \qquad (5)$$

Keeping in mind that a vector potential $\vec{A}(\vec{r})$ imprints the phase $q\hbar^{-1}\int_{\vec{r}_i}^{\vec{r}_j}\vec{A}(\vec{r})\cdot d\vec{r}$ on a particle with charge q hopping on a lattice from $\vec{r}_i$ to $\vec{r}_f$, we interpret Φ as the (dimensionless) flux of a synthetic gauge field piercing a triangle. Notice that there is no net average magnetic field as the flux piercing a hexagon is -2Φ; see Fig. 1. The flux Φ decreases monotonically from 0 to -2π with the laser amplitude g. We emphasize that in realistic implementations the photon hopping rate J is much larger than the phonon hopping rate K. It is precisely in this limit that the construction adopted here works well (with interference between direct phonon transport of amplitude K and virtual transport via the photonic route). Indeed, values for the phase all the way down to -2π can be reached, staying well within the weak-coupling limit where Eq. (5) has been derived.

In the opposite, large-bandwidth limit, $J \gg \Delta_{34}$, only a small quasimomentum region close to the $\vec{\Gamma}$ point contributes to the optically induced mechanical hopping. Away from $\vec{\Gamma}$, the OM interaction is suppressed, as the energetic distance between the lowest optical band and the mechanical bands rapidly increases. Thus, the effective mechanical hopping $K_{ij}^{(\mathrm{eff})}$ is long range in this limit, and this will change the topological properties that we discuss below. In general, the range of $K_{ij}^{(\mathrm{eff})}$ is governed by the ratio J/Δ_{34} and can be tuned by changing the gap Δ_{34} via the laser frequency.

Finally, going away from weak coupling, one can enter a regime where photon and phonon bands cross and hybridize strongly. In the following, we discuss the topological properties of the optomechanical band structure for all of these regimes.

For systems in the quantum Hall state class A, which is realized here, the topological state is uniquely identified by

the bands' Chern invariants (or TKNN invariant [2] after Thouless, Kohmoto, Nightingale and den Nijs). They are defined as the integral over the Brillouin zone of the Berry curvature of each band [2]:

$$C_l = \frac{1}{2\pi}\int_{\mathrm{BZ}} d^2k[\nabla_{\vec{k}} \times \vec{\mathcal{A}}_l(\vec{k})]\cdot\vec{e}_z, \qquad l = 1,\ldots,6. \quad (6)$$

The Berry connection $\vec{\mathcal{A}}_l = i\langle\vec{k}_l|\nabla_{\vec{k}}|\vec{k}_l\rangle$ depends on the eigenstates $|\vec{k}_l\rangle$ of Hamiltonian Eq. (4), describing hybrid excitations of photons and phonons. The full topological phase diagram calculated numerically as a function of the laser parameters is shown in Fig. 2. Whenever two (or more) bands touch, their Chern numbers may change, signaling a topological phase transition.

We start our analysis from the regime of weak coupling, when optical and vibrational bands are separated sufficiently (this regime is delimited by the dotted yellow lines in Fig. 2). For concreteness, we focus on negative detunings Δ, to the right of the diagram. At the far right, we are in the limit of nearest-neighbor hopping. There, the phonons are made to realize the kagome Chern-insulator model, with the flux Φ given by Eq. (5). In this model, all three mechanical bands are separated by complete band gaps. Both band gaps close simultaneously for special values of the flux where time-reversal symmetry is unbroken [16]. In our case, this happens when the laser is switched off, where $\Phi = 0$, and when it reaches a critical amplitude $g = g_{\mathrm{tp}} \equiv (\Delta + \Omega)\sqrt{K/J}$, where $\Phi = -\pi$. The Chern numbers are $C_{1/3} = \pm\mathrm{sgn}[\sin(\Phi)]$, $C_2 = 0$, where the bands are ordered by increasing energy [52]. Hence, a topologically nontrivial phase arises as soon as the driving is switched on, and the system changes to a different topological phase above the threshold g_{tp}. The photons also experience a synthetic gauge field, whose flux can be obtained from Eq. (5) by exchanging K and J and changing the sign. This flux is therefore small and has opposite direction. The photon band Chern numbers thus turn out to be $C_{4/6} = \mp\mathrm{sgn}[\Phi]$, $C_5 = 0$, without any transition at g_{tp}.

When the photon and phonon bands come closer by changing the laser detuning, an effective long-range hopping of phonons is induced optically, as discussed above. Then, a new topological phase appears for intermediate laser amplitudes, not predicted in the simple nearest-neighbor model. The reason is that the mechanical band gaps no longer close simultaneously but instead at two different critical couplings g_{12} and g_{23} (Fig. 2). In the previously discussed limit of short-range hopping, $J/\Delta_{34} \to 0$, these would again coalesce to become g_{tp}. The Chern numbers for long-range hopping can be computed analytically (see Appendix D).

We now turn to the regime where the photon and phonon bands overlap and interact strongly [see the center of the phase diagram Fig. 2(c)]. There, the topological phases cannot be understood any more as induced by an effective staggered synthetic gauge field for the phonons. They give rise to a phase diagram that is unique for optomechanical arrays. In this regime, a number of different phases appear. By inspecting the limit of small coupling ($g \to 0$), one notices that the topological phase transitions occur whenever bands touch at the symmetry points $\vec{\Gamma}$, $\vec{K}$, and $\vec{K}'$ or at the special points $\vec{M}_A$, $\vec{M}_B$, and $\vec{M}_C$ [see the sketch of the band structures at the phase transitions, bottom of Fig. 2(c)]. This remains true for arbitrary coupling, and can be explained as follows. Topological phase transitions can happen whenever bands touch each other (instead of repelling), which is possible if there are selection rules preventing them from interacting. At the symmetry points $\vec{k} = \vec{\Gamma}, \vec{K}, \vec{K}'$, this is guaranteed by angular momentum conservation, whereas at $\vec{M}_A$ the optical and mechanical kagome sublattice sites A are decoupled from the remaining sublattices B and C (likewise with B at $\vec{M}_B$ and C at $\vec{M}_C$). The bands actually touch simultaneously at $\vec{K}, \vec{K}'$, due to inversion symmetry, while rotational symmetry makes them touch simultaneously at $\vec{M}_A$, $\vec{M}_B$, and $\vec{M}_C$. From these considerations, we can predict the transitions to occur at the laser detunings $\Delta + \Omega \approx -4J, -2J, -J, 0, 2J$, for small coupling g and small mechanical hopping K. The resulting set of Chern numbers for all six bands is displayed in Fig. 2, for each of the various topological phases.

D. Chiral edge state transport

A fundamental consequence of the topological nature of the optomechanical band structure is the appearance of chiral edge states at the boundaries of a finite-size system. These excitations are topologically protected against scattering if the bands are separated by a complete band gap. They are thus very distinct from the type of edge states that are produced in graphene-type systems with Dirac dispersion, which are not robust against disorder and whose existence even depends on the details of the boundary. The net number of such edge states (right movers minus left movers) within a given band gap is directly determined by the sum of the Chern numbers of all lower-lying bands. While in the effective short-range kagome model each pair of subsequent bands is separated by such a gap, this is not generally true in the full optomechanical model. Large gaps are desirable because they are more robust against dissipation, disorder, and Stokes scattering, described by additional terms $\hat{H}_{\mathrm{st}} = -\hbar(g_j\hat{a}_j^\dagger\hat{b}_j^\dagger + \mathrm{H.c.})$ in the Hamiltonian. However, topological band gaps cannot be larger than the mechanical bandwidth $\sim K$, since they arise by the interplay of intrinsic and optically induced hopping; see Appendix E. For example, in the realistic regime where the optical bandwidth is larger than the mechanical frequency, the largest topological gap ω_{gap} is given by $\omega_{\mathrm{gap}} \approx g\sqrt{2J/K}$ (we consider a laser drive at the mechanical red sideband of the lowest frequency optical

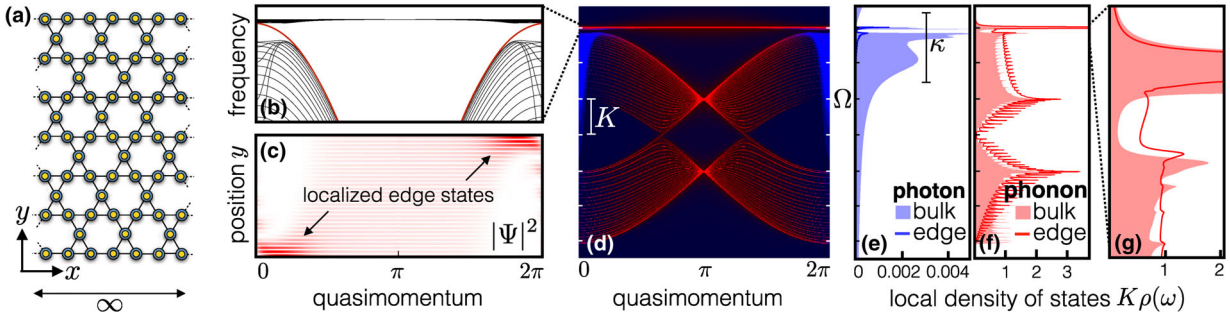

FIG. 3. Edge states in a kagome optomechanical array. (d) Band structure in the center of a finite-width strip, whose geometry is shown in (a), as a function of the wave number along the longitudinal direction of the strip. Blue (red) indicates large photonic (phononic) components. Optical and mechanical dissipation, as well as the Stokes interaction, have all been included (see Appendix F). The indicated band gap is of topological nature. (b) Zoom-in of the strip's band structure (here for clarity without dissipation). The dispersion of the edge states is highlighted. The corresponding phonon probability density as a function of position across the strip is shown in (c), demonstrating localization at the edges for quasimomenta where the frequency lies in the bulk band gap. The photonic component (not shown) is small. (e),(f) Local density of states for photons and phonons, respectively, both in the bulk and at the edge of such a strip (of 30 unit cell width). The band gap is much smaller than the photon decay rate κ. (g) Zoom-in of the phonon local density of states. The parameters are $\Omega = 0.1J$, $\Delta = -4.02J$, $K = 0.005J$, $g = 0.007J$, $\kappa = 0.01J$, and $\gamma = 8 \times 10^{-5}J$.

mode); see Appendix E. In order to show the feasibility of a topological optomechanical array, we include all of these aspects in the remainder of the paper, with a photon decay rate κ and a mechanical damping rate γ; see Appendixes A and F. In Fig. 3, we show that for realistic parameters the topological gaps are surprisingly resilient to dissipation. The bulk band structure in Fig. 3(d) has a topological gap between the second band (a hybrid photon-phonon band) and the third band. The band gaps in the bulk photon and phonon LDOS, shown in Figs. 3(e) and 3(f) are weakly smeared by dissipation, although the band gap is much smaller than the photon decay rate κ. Such a robustness, which is related to the optomechanically induced transparency phenomenon [56–58], has been noticed in a different context already for a 1D optomechanical array [49]. It occurs because the excitations of the hybrid band have strong phononic components at the band edge, making them less sensitive to photon decay; see the color code in Fig. 3(d). In a strip of finite width (30 unit cells), one can observe that the phononic wave functions form well-localized chiral edge states [Figs. 3(b) and 3(c)]. The residual bulk DOS inside the band gap [in Figs. 3(f) and 3(g)] is produced when the mechanical dissipation smears the nearby large peak in the DOS (the height of this peak is larger by a factor of $\approx$1600 than the residual bulk DOS inside the band gap). That peak is formed by the localized excitations in the flat mechanical band of the kagome lattice. We have checked that the transport is still chiral even in the presence of such residual bulk DOS; see Appendix G. Our analysis shows that the coupling to the localized excitations causes injection losses but not backscattering.

Finally, we study transport in a finite-size array, for an experimentally realistic setting that reveals the robustness against backscattering by disorder. Additional robustness against mechanical dissipation in the form of clamping losses can be provided by engineering "phonon shields," as demonstrated in Ref. [37]. Since the gapless excitations at the sample edge are phononic in nature, they could be excited by applying local oscillating stress. On the other hand, in the current setting, it is experimentally most straightforward to shine light on the sample edge. Even though the *photon* states are not localized at the edge (unlike the *phonon* edge modes), this simple approach works surprisingly well. Effectively, the beat note between the weak, local probe laser and the strong, global driving laser creates an oscillating radiation pressure force, launching phonons. In Fig. 4, we show a simulation of topologically protected chiral sound waves excited locally by a laser, traveling along the sample edge around an obstruction. In addition, we have checked that moderate random on-site disorder also does not affect the transport. Moreover, it turns out that spatially resolved imaging of the light field emanating from the sample [Fig. 4(a)] can be used to map out the phonon edge state. This is because the local vibrations will imprint sidebands on the strong drive laser, and one of these sidebands appears at the probe laser frequency, which then can be spectrally filtered and imaged.

In the strong-coupling regime discussed above, where photons and phonons mix completely, one obtains chiral transport of photon-phonon polariton excitations, which can also be excited and read out in the manner discussed here.

The phonons will eventually decay, since the topological protection prevents disorder-induced backscattering but not dissipation (the same is true as well for all topological photon systems, for example). The number of sites over which the phonons propagate along the chiral edge state is given by their speed (the slope of the edge state dispersion) divided by the overall mechanical decay rate (including both intrinsic and optically induced dissipation). In the

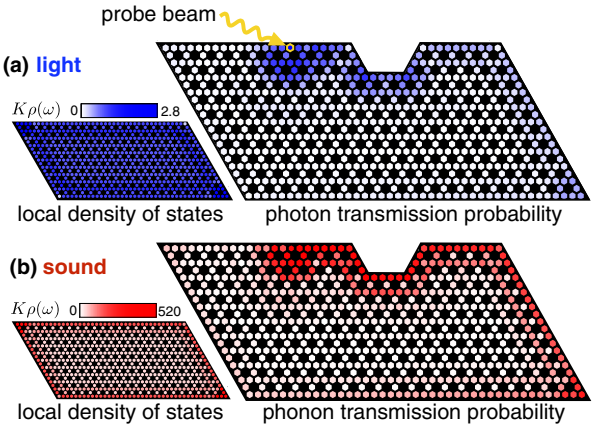

FIG. 4. Simulation of transport in a finite system. A probe laser is injected locally at a site on the sample edge, at a fixed frequency, launching phonons that are transported along the chiral edge state. The larger figures depict the probability map of finding a photon (a) or a phonon (b), demonstrating transmission around an obstacle. Because of the optomechanical interaction, the light intensity in (a), which could be imaged locally, represents a faithful probe of the chiral phonon transport in (b). The probe frequency lies in a bulk band gap ($\omega_L - \omega_{\rm probe} = 1.06J$) that just permits mechanical edge states. The parameters correspond to large detuning between optical and mechanical bands ($\Delta/J = -5.7$, $\Omega/J = 1$, $g/J = 0.2$, $K/J = 0.05$, $\kappa/J = 0.1$, and $\gamma/J = 0.002$).

simplest case, the typical scale of the propagation length is given by the ratio of the mechanical hopping K over the mechanical decay rate γ. For parameters compatible with state-of-the-art devices, the phonons can propagate for about 100 sites before decaying; see Appendix G for a more detailed analysis. This is completely sufficient for connecting phonon reservoirs and other applications in phononics.

We now address briefly the most relevant issues for the experimental realization of optomechanical Chern insulators. The most important constraint in our model is the need to avoid a mechanical lasing instability [33] that may appear for larger bandwidths ($J > \Omega/3$) due to the Stokes terms. For laser frequencies below the blue sideband of the lowest frequency optical mode, the instability threshold is reached when the cooperativity equals (see Appendix H)

$$\mathcal{C} \equiv 4\frac{g^2}{\kappa\gamma} = 1 + \left(\frac{\Delta + 4J - \Omega - 2K}{\kappa/2}\right)^2. \qquad (7)$$

The laser intensity (proportional to g^2) therefore has to remain below this threshold, which is accounted for when selecting parameters in our simulation results displayed here.

Regarding experimental parameters, in general, in our figures we remain compatible with those of the recent 2D snowflake crystal single-defect experiment [38,55], where they report $\Omega \approx 2\pi \times 9$ GHz and a single-photon coupling strength of $g_0 \approx 2\pi \times 250$ kHz. To obtain the $g = g_0\sqrt{n_{\rm phot}}$ employed in Fig. 3 (where we assume $J = 10\ \Omega$ and $g = 0.007J$) would require on the order of $n_{\rm phot} \sim 10^6$ circulating photons. Although challenging, this should be doable, especially since any possible increase of the phonon number due to unwanted heating (and finite temperatures in general) does not affect measurements of the band structure and transmission amplitudes, since the fluctuations do not contribute to the average signal amplitudes.

In all future experiments on transport in optomechanical arrays, it will be important to minimize disorder due to fabrication fluctuations, and efforts to characterize and optimize this are only now starting. In particular, post-fabrication processing techniques, such as local oxidation [59], can be employed in the future in order to drastically reduce the disorder by orders of magnitude. In numerical simulations, we have seen that the topological effects persist robustly up to disorder strengths of 2% of Ω in the mechanical on-site frequencies and up to about J in the optical on-site frequencies (at $J = 10\ \Omega$). More generally, we observe in our simulations that there is a wide latitude in parameter combinations to obtain the effects discussed here. For example, it may be more convenient experimentally to use larger photon hopping rates J. Then, the instability is reached for smaller g, the band gaps are smaller, and the edge states' penetration length is larger. We checked that for $J = 100\ \Omega$ and $g = 5 \times 10^{-2}\ \Omega$ (and the other parameters in the same range as Fig. 3), one can still find a topological band gap. The corresponding edge states are well localized on a strip of width 60 unit cells.

III. CONCLUSION

Apart from its fundamental interest, chiral phonon transport, robust against disorder, could be useful for many settings. Among them are the transport of phonons between localized long-lived vibrational modes (forming robust "phononic networks") and the study of quantized heat transport [60] in an unconventional setting (with a "one-way" connection between heat reservoirs). The realization of a phonon Chern insulator would thus also enable the observation of new physical phenomena relevant to phononics. In addition, the mechanism we employ is conceptually distinct from anything that has been considered for photons, to the best of our knowledge. In fact, the optomechanical route towards Chern insulators has major advantages over other proposals that have been put forward for photons and which one might try to translate to phonons: The optomechanical concept is more flexible than geometry-based approaches [17,23], since the properties can be tuned quickly *in situ*, and in contrast to settings based on local electrical modulation [19], it does not require local wiring of any kind (which is hard to scale up).

The flexibility of the approach proposed here, where the pattern of the laser field determines the band structure, could be exploited to generate more general layouts *in situ*,

where arbitrarily shaped regions of different topological phases are produced, studying the transport through the edge states that form at their interfaces, possibly arranged in interesting interferometer configurations. Moreover, the time-dependent local control of the band structure could be the basis for quench experiments on topological phases of light and sound. Finally, if future improvements in the coupling g_0 between single photons and phonons were to permit entering the strong single-photon coupling regime (with $g_0 \sim \kappa, g_0 \sim \Omega$), optomechanical fractional Chern insulators could be realized, being governed by strong quantum correlations.

ACKNOWLEDGEMENTS

We acknowledge support by the ERC Starting Grant OPTOMECH, by the DARPA project ORCHID, and by the European Marie-Curie ITN network cQOM. We thank Aashish Clerk, Alexander Altland, and Oskar Painter for discussions.

APPENDIX A: DERIVATION OF THE LINEARIZED HAMILTONIAN FOR THE KAGOME OPTOMECHANICAL ARRAY

We start from the standard input-output formalism for an array of optomechanical cells (each consisting of a vibrational and an optical mode) on a kagome lattice, driven by a laser with uniform intensity and a pattern of phases φ_j. As we intend to linearize around the classical solution, we first write down the equations of motion for the classical fields (the quantum fields averaged over quantum and classical fluctuations) in a frame rotating with the drive:

$$\begin{aligned}\dot{\beta}_j &= (-i\Omega-\gamma/2)\beta_j + ig_0|\alpha_j|^2 + iK\sum_{\langle l,j\rangle}\beta_l,\\ \dot{\alpha}_j &= (i\Delta^{(0)}-\kappa/2)\alpha_j + i2g_0\alpha_j \mathrm{Re}\beta_j + iJ\sum_{\langle l,j\rangle}\alpha_l\\ &\quad + \sqrt{\kappa}e^{i\varphi_j}|\alpha^{(\mathrm{in})}|.\end{aligned} \tag{A1}$$

Here, $j=(n,m,s)$, $n,m\in Z$, $s=A,B,C$, and $\langle j,l\rangle$ indicates the sum over nearest-neighbor sites. Moreover, g_0 is the shift of the optical frequencies due to a single phonon (more precisely, a zero-point displacement), K (J) is the phonon (photon) hopping rate, and γ (κ) is the phonon (photon) decay rate. The laser detuning is $\Delta^{(0)}=\omega_L-\omega^{(0)}_{\mathrm{phot}}$, and $|\alpha^{(\mathrm{in})}|$ is the absolute value of the driving field. The phases φ_i are independent of the unit cell, but they depend on the sublattice site: $\varphi_B-\varphi_A=\varphi_C-\varphi_B=\varphi_A-\varphi_C=2\pi/3$. Then, the stationary solutions of Eq. (A1) are given by $\alpha_A=e^{-i2\pi/3}\alpha_B=e^{i2\pi/3}\alpha_C$, where α_A is a solution of the third-order polynomial equation:

$$\alpha_A=\frac{ie^{i\varphi_A}\sqrt{\kappa}\alpha^{(\mathrm{in})}}{\Delta^{(0)}+4J+2g_0^2|\alpha_A|^2/(\Omega-4K)+i\kappa/2}. \tag{A2}$$

Without loss of generality, we can choose the phase of $\alpha^{(\mathrm{in})}$ to fix $\alpha_A>0$ real valued (this amounts to a gauge transformation).

We now linearize the quantum Langevin equations (input-output equations of motion) around the classical solutions. We find (where $\hat{H}'=\hat{H}+\hat{H}_{\mathrm{st}}$ contains also the Stokes interaction terms):

$$\begin{aligned}\dot{\hat{b}}_j &= i\hbar^{-1}[\hat{H}',\hat{b}_j]-\gamma\hat{b}_j/2+\sqrt{\gamma}\hat{b}_j^{(\mathrm{in})}\\ &= (-i\Omega-\gamma/2)\hat{b}_j+ig_j^*\hat{a}_j+ig_j\hat{a}_j^\dagger+iK\sum_{\langle l,j\rangle}\hat{b}_l+\sqrt{\gamma}\hat{b}_j^{(\mathrm{in})},\\ \dot{\hat{a}}_j &= i\hbar^{-1}[\hat{H}',\hat{a}_j]-\kappa\hat{a}_j/2+\sqrt{\kappa}\hat{a}_j^{(\mathrm{in})}\\ &= (i\Delta-\kappa/2)\hat{a}_j+ig_j(\hat{b}_j+\hat{b}_j^\dagger)+iJ\sum_{\langle l,j\rangle}\hat{a}_l+\sqrt{\kappa}\hat{a}_j^{(\mathrm{in})},\end{aligned} \tag{A3}$$

where $g_A=g_0\alpha_A=e^{-i2\pi/3}g_B=e^{i2\pi/3}g_C$, and the detuning Δ includes a small shift of the optical resonances due to the average mechanical displacement induced by the radiation pressure: $\Delta=\Delta^{(0)}+2g_0^2|\alpha_A|^2/(\Omega-4K)$. The input fields $\hat{b}_j^{(\mathrm{in})}$ and $\hat{a}_j^{(\mathrm{in})}$ describe the vacuum (and possibly, thermal) fluctuations. The Hamiltonian $\hat{H}$ is given in Eq. (1) of the main text, and together with the Stokes terms, $\hat{H}_{\mathrm{st}}=-\hbar(g_j\hat{a}_j^\dagger\hat{b}_j^\dagger+\mathrm{H.c.})$, it produces the right-hand side of the Langevin equations displayed here (except the fluctuation and decay terms, which stem from the interaction with the vibrational and electromagnetic environment).

APPENDIX B: SYMMETRIES OF THE KAGOME LATTICE

The topological effects discussed in the main text do not depend qualitatively on the details of the hopping interactions (there, for concreteness, we assume that only nearest-neighbor sites are coupled) provided that the underlying inversion symmetry (around a corner of the triangle forming the unit cell) and the $\mathcal{C}_3$ rotational symmetry of the kagome lattice are retained. This applies, in particular, to the topological phase diagram in Fig. 2. In our model, a topological phase transition occurs when two bands touch (instead of repelling) as a result of a selection rule. This happens at the symmetry points $\vec{\Gamma}$, $\vec{K}$, and $\vec{K}'$, where only three transitions are allowed by the C_3 symmetry: $|M,\oslash\rangle\leftrightarrow|O,\circlearrowleft\rangle$, $|M,\circlearrowleft\rangle\leftrightarrow|O,\circlearrowright\rangle$, and $|M,\circlearrowright\rangle\leftrightarrow|O,\oslash\rangle$. Moreover, two bands can touch at the special points $\vec{M}_A$, $\vec{M}_B$, and $\vec{M}_C$, where the inversion symmetry ensures that the optical and mechanical kagome sublattices A, B, or C, respectively, are decoupled from the remaining sublattices.

When these symmetries are broken, the phase diagram becomes qualitatively different. For instance, unequal mechanical and/or optical eigenfrequencies on the different sublattices break the $\mathcal{C}_3$ symmetry. This symmetry breaking has a twofold effect. First, the bands do not touch anymore at the symmetry points $\vec{\Gamma}$, $\vec{K}$, and $\vec{K}'$. This first effect does not change qualitatively the phase diagram when a small perturbation breaks the symmetry. In this case, the bands touch in the neighborhood of $\vec{\Gamma}$, $\vec{K}$, and $\vec{K}'$, and the borders of the corresponding topological phase transitions are only slightly deformed. Second, the bands do not touch simultaneously at $\vec{M}_A$, $\vec{M}_B$, and $\vec{M}_C$. Then, the border of the corresponding topological phase transitions split into three lines and new topological phases appear. This second effect induces a qualitative change of the topological phase diagram even when only a small perturbation breaks the symmetry.

APPENDIX C: DERIVATION OF THE EFFECTIVE TIGHT-BINDING PHONON HAMILTONIAN FOR LARGE DETUNINGS

Our aim in this section is to integrate out the optical field and derive the effective Hamiltonian for the phonons. Various ways exist for doing this, and here we choose to eliminate the optical fields from the equations of motion. In this section, we consider the regime of nearest-neighbor effective phonon hopping at the far right and far left of the phase diagram in Fig. 2. For concreteness, we focus on the far right region in the diagram, $-\Delta-\Omega \gg J$. Since we want to also include Stokes processes, we start from the linearized Hamiltonian, Eq. (1). Keeping in mind that the optical backaction is filtered by the mechanical band, it is convenient to divide $\hat{a}_j$ into its sidebands:

$$\hat{a}_j \equiv e^{-i\Omega t}\hat{a}_j^{(\mathrm{red})} + e^{i\Omega t}\hat{a}_j^{(\mathrm{blue})} + \delta\hat{a}. \tag{C1}$$

When the mechanical bandwidth is small, i.e., when $6K^{(\mathrm{eff})} \ll \Omega$ (where $K^{(\mathrm{eff})}$ is calculated below), $a_{\mathrm{red}}(t)$ and $a_{\mathrm{blue}}(t)$ are slowly varying functions (as is $\delta\hat{a}$, describing the intrinsic optical fluctuations), and one can neglect their time derivative in the Heisenberg equation $\dot{\hat{a}}_j = i\hbar^{-1}[\hat{H}, \hat{a}_j]$. We find

$$\begin{aligned} e^{-i\Omega t}\hat{a}_j^{(\mathrm{red})} &= -\frac{g_j}{\Delta+\Omega}\hat{b}_j + \sum_{\langle j,l\rangle}\frac{Jg_l}{(\Delta+\Omega)^2}\hat{b}_l, \\ e^{i\Omega t}\hat{a}_j^{(\mathrm{blue})} &= -\frac{g_j}{\Delta-\Omega}\hat{b}_j^\dagger + \sum_{\langle j,l\rangle}\frac{Jg_l}{(\Delta-\Omega)^2}\hat{b}_l^\dagger. \end{aligned} \tag{C2}$$

We eliminate the photons by substituting Eqs. (C1) and (C2) in the Heisenberg equation $\dot{\hat{b}}_j = i\hbar^{-1}[\hat{H}, \hat{b}_j]$ and arrive at $\dot{\hat{b}}_j = i\hbar^{-1}[\hat{H}_{\mathrm{eff}}, \hat{b}_j]$, where

$$\frac{\hat{H}_{\mathrm{eff}}}{\hbar} \approx \sum_j \Omega^{(\mathrm{eff})}\hat{b}_j^\dagger\hat{b}_j - \sum_{\langle j,l\rangle} K_{jl}^{(\mathrm{eff})}\hat{b}_j^\dagger\hat{b}_l, \tag{C3}$$

$$\Omega^{(\mathrm{eff})} = \Omega + \frac{g^2}{(\Delta+\Omega)} + \frac{g^2}{(\Delta-\Omega)}, \tag{C4}$$

$$K_{jl}^{(\mathrm{eff})} = K + J\frac{g_j^* g_l}{(\Delta+\Omega)^2} + J\frac{g_j g_l^*}{(\Delta-\Omega)^2}. \tag{C5}$$

In deriving this, we neglect the terms containing two creation or annihilation operators (of the parametric oscillator type $\hat{b}^\dagger\hat{b}^\dagger$, etc.), which is a good approximation for a small bandwidth $6K^{(\mathrm{eff})} \ll \Omega^{(\mathrm{eff})}$. The third term on the right-hand side of Eq. (C5) describes the additional hopping amplitude induced by Stokes scattering (going beyond the simpler approximation discussed in the main text, where this term is neglected). The corresponding flux is

$$\Phi = -\frac{3\pi}{2} - 3\arctan\frac{K(\Delta+\Omega)^2(\Delta-\Omega)^2 - Jg^2(\Delta^2+\Omega^2)}{-2\sqrt{3}Jg^2\Omega\Delta}.$$

The above result tends to the expression in Eq. (3) (which does not include Stokes scattering) for $|\Delta+\Omega| \ll \Omega$. From this formula it is easy to prove that the small correction due to the Stokes processes decreases the flux if $\Phi < -\pi$, but it increases it if $\Phi > -\pi$. Since both mechanical band gaps reach a maximum width at $\Phi = -\pi/2$ and $\Phi = -3\pi/2$, the Stokes processes enlarge the gap in the broad parameter regime $-3\pi/2 < \Phi < -\pi/2$.

APPENDIX D: CALCULATION OF THE CHERN NUMBERS AND THE CRITICAL COUPLINGS IN THE WEAK-COUPLING REGIME

1. Critical couplings

In the limit of a very large separation between optical and mechanical bands, we have a model of phonons with effective nearest-neighbor hopping on a Kagome lattice, and there is only one critical coupling for a topological phase transition. When the separation is reduced, longer-range hopping develops, and the first effect is that another topological phase shows up. It is bounded by two critical couplings, g_{12} and g_{23}. These can be calculated by diagonalizing the single-particle Hamiltonian Eq. (2) at the symmetry points $\vec{\Gamma}$ and $\vec{K}'$ (the inversion symmetry ensures that the second and third band will touch simultaneously at $\vec{K}$ and $\vec{K}'$). Because of rotational symmetry there are only three allowed transitions at the symmetry points: $|M,\oslash\rangle \leftrightarrow |O,\circlearrowleft\rangle$, $|M,\circlearrowleft\rangle \leftrightarrow |O,\circlearrowright\rangle$, and $|M,\circlearrowright\rangle \leftrightarrow |O,\oslash\rangle$. Hence, the Hamiltonian is block diagonal with three 2×2 blocks and can be very easily diagonalized for arbitrary g. However, this leads to a nonlinear equation for the border of the phase transitions g_{12} and g_{23}. Instead, we restrict

ourselves to the weak-coupling regime (limit of large separation between optical and mechanical bands), where it is possible to find simple analytical expressions for the critical couplings and to calculate the Chern numbers analytically.

At the $\vec{\Gamma}$ point, the spectrum of the single-particle Hamiltonian Eq. (2) is (up to leading order in g)

$$E_{O\circlearrowright} = -\Delta + 2J + \frac{g^2}{-\Delta + 2J - \Omega - E_{M\circlearrowleft}},$$
$$E_{M\circlearrowleft} = \Omega + 2K + \frac{g^2}{\Delta - 2J + \Omega},$$
$$E_{O\circlearrowleft} = -\Delta + 2J + \frac{g^2}{-\Delta + 2J - \Omega - E_{M\oslash}},$$
$$E_{M\oslash} = \Omega - 4K + \frac{g^2}{\Delta - 2J + \Omega},$$
$$E_{O\oslash} = -\Delta - 4J, \qquad E_{M\circlearrowright} = \Omega + 2K + \frac{g^2}{\Delta + 4J + \Omega}.$$

Here, we indicate with $E_{O\circlearrowright}$ the eigenvalue corresponding to eigenvector $|\circlearrowright, O\rangle + \alpha|\circlearrowleft, M\rangle$ (with $\alpha \propto g$), and likewise for the other eigenvalues. The above eigenvalues, ordered by increasing energy, are (for small g)

$$E_1 = E_{M\oslash}, \quad E_2 = E_{M\circlearrowright}, \quad E_3 = E_{M\circlearrowleft},$$
$$E_4 = E_{O\oslash}, \quad E_5 = E_{O\circlearrowleft}, \quad E_6 = E_{O\circlearrowright}.$$

The coupling g_{12}, where the first and the second mechanical band touch each other, can be obtained from the condition $E_{M\oslash} = E_{M\circlearrowright}$, yielding

$$g_{12} = \{6K[(\Delta - 2J + \Omega)^{-1} - (\Delta + 4J + \Omega)^{-1}]^{-1}\}^{1/2}.$$

Above this threshold, the first and second band exchange their eigenvectors:

$$E_1 = E_{M\circlearrowright}, \quad E_2 = E_{M\oslash}, \quad E_3 = E_{M\circlearrowleft},$$
$$E_4 = E_{O\oslash}, \quad E_5 = E_{O\circlearrowleft}, \quad E_6 = E_{O\circlearrowright}. \tag{D1}$$

The same calculation at the $\vec{K}'$ point gives

$$E_{O\circlearrowright} = -\Delta + 2J, \qquad E_{M\circlearrowleft} = \Omega - K + \frac{g^2}{\Delta - 2J + \Omega},$$
$$E_{O\circlearrowleft} = -\Delta - J + \frac{g^2}{-\Delta - J - \Omega - E_{M\oslash}},$$
$$E_{M\oslash} = \Omega - K + \frac{g^2}{\Delta + J + \Omega},$$
$$E_{O\oslash} = -\Delta - J + \frac{g^2}{-\Delta - J - E_{M\circlearrowright}},$$
$$E_{M\circlearrowright} = \Omega + 2K + \frac{g^2}{\Delta + J + \Omega}.$$

In this case, the eigenvalues ordered by increasing energy for small g are

$$E_1 = E_{M\oslash}, \quad E_2 = E_{M\circlearrowleft}, \quad E_3 = E_{M\circlearrowright},$$
$$E_4 = E_{O\circlearrowleft}, \quad E_5 = E_{O\oslash}, \quad E_6 = E_{O\circlearrowright}. \tag{D2}$$

The coupling g_{23}, where the second and third band touch each other, can be obtained from the condition $E_{M\circlearrowright} = E_{M\circlearrowleft}$, yielding

$$g_{23} = \{3K[(\Delta - 2J + \Omega)^{-1} - (\Delta + J + \Omega)^{-1}]^{-1}\}^{1/2}.$$

In the same way, at the K point and for $g < g_{23}$, we have

$$E_1 = E_{M\circlearrowright}, \quad E_2 = E_{M\oslash}, \quad E_3 = E_{M\circlearrowleft},$$
$$E_4 = E_{O\oslash}, \quad E_5 = E_{O\circlearrowright}, \quad E_6 = E_{O\circlearrowleft}. \tag{D3}$$

Also at this point the second and third bands swap their eigenstates at the critical coupling g_{23}.

2. Chern numbers

In the weak-coupling regime, it is also possible to compute the Chern numbers analytically. We show this explicitly for the phase that develops due to longer-range phonon hopping, i.e., the phase discussed above between g_{12} and g_{23}. We follow Ref. [61]. Applying their general idea, we initially try to fix the gauge by requiring $(\langle M, \circlearrowleft| + \langle O, \circlearrowright|)|\vec{k}, l\rangle \in \mathbb{R}$, where $|\vec{k}, l\rangle$ is the eigenstate of band l at $\vec{k}$. If such a gauge were well defined over the whole Brillouin zone, the Chern number would be 0 [in Eq. (4), one integrates the curl of a smooth function over a torus, which gives zero from the Stokes theorem]. However, there are *obstructions* preventing us from defining a global gauge. At an obstruction, the overlap $(\langle M, \circlearrowleft| + \langle O, \circlearrowright|)|\vec{k}, l\rangle$ vanishes and the chosen gauge is ill defined. In its neighborhood, i.e., a finite region within the Brillouin zone, one has to choose a different gauge. In the new local gauge, the overlap $(\langle M, \circlearrowleft| + \langle O, \circlearrowright|)|\vec{k}, l\rangle \equiv \rho(\vec{k})e^{-i\theta(\vec{k})}$ is a smooth function of $\vec{k}$ and its complex argument winds an integer number of times n on a path around the obstruction, $n = (2\pi)^{-1}\oint \vec{\nabla}\theta(\vec{k}) \cdot d\vec{k}$. When calculating the Chern number, one picks up a contribution from the boundary between the two regions of different gauge. The band Chern number turns out to be the sum of the winding numbers for all obstructions: $C_l = \sum_i n_i^{(l)}$. Such an analytical approach is possible because, in the weak-coupling limit and for our particular choice of gauge, obstructions form only at the symmetry points (this does not hold in the strong coupling limit).

For concreteness, we focus on the second band and on the topological phase introduced by the effective long-range hopping. As discussed above, in this phase (corresponding to $g_{12} < g < g_{23}$), the second band wave function is state $|M, \oslash\rangle$ (with a small admixture to $|O, \circlearrowleft\rangle$) at the $\vec{\Gamma}$ point, state $|M, \circlearrowleft\rangle$ (with a small admixture to $|O, \circlearrowright\rangle$) at the $\vec{K}'$ point, and state $|M, \circlearrowright\rangle$ (with a small admixture to

$|O,\oslash\rangle$) at the $\vec{K}$ point. Hence, for the second band, and for the global gauge defined above, there are obstructions at $\vec{k}=\vec{\Gamma},\vec{K}$.

From the above discussion it is clear that in order to compute the Chern number of the second band, it is sufficient to compute the overlap $(\langle M,\circlearrowleft|+\langle O,\circlearrowright|)|\vec{k},2\rangle$ close to the symmetry points $\vec{\Gamma}$ and $\vec{K}$. We start from $\vec{\Gamma}$. We decompose the Hamiltonian into $\hat{H}(\vec{\Gamma}+\delta\vec{k})=\hat{H}(\vec{\Gamma})-(\bar{t}+\delta t\hat{\sigma}_z/2)\delta\hat{\tau}_{\vec{\Gamma}}(\delta\vec{k})$,

$$\delta\hat{\tau}_{\vec{\Gamma}}(\delta\vec{k})=i\begin{pmatrix}0 & -\delta\vec{k}\cdot\vec{a}_1 & \delta\vec{k}\cdot\vec{a}_3\\ \delta\vec{k}\cdot\vec{a}_1 & 0 & -\delta\vec{k}\cdot\vec{a}_2\\ -\delta\vec{k}\cdot\vec{a}_3 & \delta\vec{k}\cdot\vec{a}_2 & 0\end{pmatrix}, \quad \text{(D4)}$$

where $\delta\vec{k}=\vec{k}-\vec{\Gamma}$. From Eqs. (D4) and (D1) we find, using standard perturbation theory in $\delta\vec{k}$,

$$(\langle O,\circlearrowright|+\langle M,\circlearrowleft|)|\hat{k},2\rangle\propto\langle\circlearrowleft|\delta\hat{\tau}_{\vec{\Gamma}}(\delta\vec{k})|\oslash\rangle\propto\delta k_x-i\delta k_y.$$

Hence, the phase increases by 2π on a small path going anticlockwise around the obstruction: the winding number is 1. In a neighborhood of $\vec{K}$, we decompose the Hamiltonian into $\hat{H}(\vec{K}+\delta\vec{k})=\hat{H}(\vec{K})-(\bar{t}+\delta t\hat{\sigma}_z/2)\delta\hat{\tau}_{\vec{K}}(\delta\vec{k})$,

$$\delta\hat{\tau}_{\vec{K}}(\delta\vec{k})=i\begin{pmatrix}0 & -e^{i2\pi/3}\delta\vec{k}\cdot\vec{a}_1 & e^{-i2\pi/3}\delta\vec{k}\cdot\vec{a}_3\\ e^{-i2\pi/3}\delta\vec{k}\cdot\vec{a}_1 & 0 & -e^{i2\pi/3}\delta\vec{k}\cdot\vec{a}_2\\ -e^{i2\pi/3}\delta\vec{k}\cdot\vec{a}_3 & e^{-i2\pi/3}\delta\vec{k}\cdot\vec{a}_2 & 0\end{pmatrix}. \quad \text{(D5)}$$

From Eqs. (D2) and (D5), we find

$$(\langle O,\circlearrowright|+\langle M,\circlearrowleft|)|\vec{k},2\rangle\propto\langle\circlearrowright|\delta\hat{\tau}_{\vec{K}}(\delta\vec{k})|\circlearrowleft\rangle\propto\delta k_x-i\delta k_y.$$

Notice that in this case the overlap comes from the optical part of the wave function. From the above expression we see that the winding number is again 1. We can conclude that the Chern number for the second band in the phase introduced by the long-range hopping (between g_{12} and g_{23}) is 2. A similar calculation shows that the first band has obstructions at $\vec{\Gamma}$ and $\vec{K}$ with winding number -1 and an obstruction at $\vec{K}'$ with winding number 1, whereas the third band has an obstruction with winding number -1 at $\vec{K}'$. Hence, the Chern numbers for the mechanical bands in the long-range hopping phase are $[-1,2,-1]$. When the first and second bands touch for $g=g_{12}$ at $\vec{\Gamma}$, the wave functions change smoothly, but they swap the bands. Hence, below g_{12}, the corresponding obstructions with their winding numbers are also swapped and we recover the result for small fluxes in the tight-binding model: $[1,0,-1]$. A similar argument shows that, for the Chern numbers for $g>g_{23}$, we recover the result for large fluxes in the tight-binding model: $[-1,0,1]$.

APPENDIX E: SIZE OF THE BAND GAPS

The chiral excitations at the edge of the sample are more robust against dissipation and disorder in the presence of large band gaps. In Fig. 5, we show the largest band gap as a function of the laser parameters.

Large band gaps of the order $\sim K$ are present for comparatively large values of g, $g\gg K$. It is easy to understand this behavior: for $K=0$, time-reversal symmetry is not broken as one can eliminate the pattern of phases in the couplings g_i by a gauge transformation on the phonon fields. In that case, all Chern numbers turn out to be zero and there is no topologically nontrivial band gap. In the presence of a small K, complete band gaps open. Since

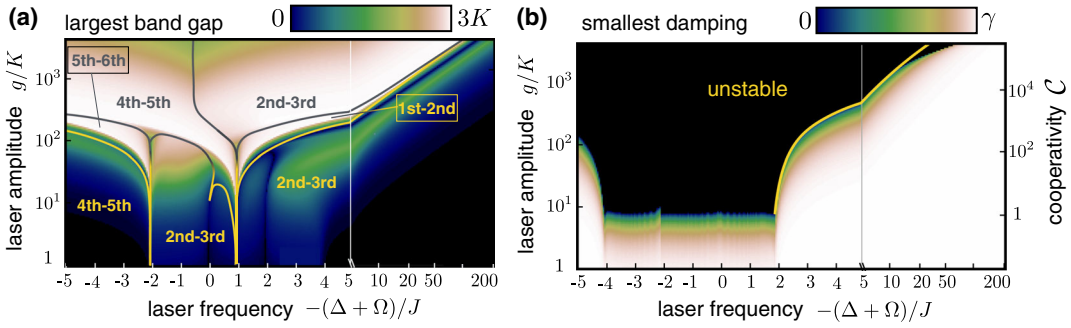

FIG. 5. (a) Plot of the largest complete topologically nontrivial band gap as a function of the laser parameters for $K/J=10^{-3}$. The yellow lines divide the diagram in separate parameter regions. The largest band gap lies between the subsequent bands indicated inside each region. This diagram does not depend on Ω. (b) Stability diagram for $J/\Omega=1$, $\gamma=0.002J$, and $\kappa=0.1J$. It shows the damping rate of the slowest relaxation process. The unstable region where the Green function $\tilde{G}(\omega,l,j)$ has a pole in the upper-half plane is marked in black. The mechanical lasing threshold of Eq. (H2) is plotted in yellow, in its region of validity. Note that the onset of the mechanical lasing instability (and that of another parametric instability visible in the top right-hand corner) restricts the region where the system is stable. We emphasize that the stable region will include the whole parameter range displayed in Fig. 2(c) for a sufficiently large value of Ω [where Ω was not specified for Fig. 2(c), since that figure is independent of Ω].

K is the smallest frequency scale, the band gaps can be computed by perturbation theory in K and are of order $\lesssim K$. For example, in the limit of effective tight-binding phonon hopping (optical bands well separated from mechanical bands), large band gaps are reached for $\Phi = 3/2$, where the size of the two mechanical band gaps is $3K$.

It is also possible to estimate the band gap in the more promising parameter regime where the optical bandwidth is large, $J \gtrsim \Omega$. In this case, it is advantageous to choose the laser frequency such that an optical band gets close but does not cross the mechanical band, $\Omega \gg -\Delta - 4J - \Omega > 0$. In this regime, the modes in the lower optical band and with quasimomentum $k \ll 1$ interact most strongly with the mechanics. In fact, all other optical modes are far detuned due to the steep optical dispersion. Near $k = 0$ (the Γ point), the low-frequency optical modes have approximately zero quasiangular momentum. For a sideband resolved system, we can do a rotating wave approximation (since the blue sideband of the low-frequency optical modes is detuned by 2Ω). Since a photon with zero-quasiangular momentum is converted into a phonon with unit angular momentum (the additional quasimomentum comes from the laser drive), only such a mechanical mode is coupled to the light. Moreover, at the Γ point the mechanical states with quasiangular momentum ± 1 are quasidegenerate. Thus, in order to compute the band gap formed close to the Γ point by the optomechanical interaction, we can neglect the influence of the remaining modes and project Hamiltonian Eq. (4) into these three levels. In a frame rotating with frequency $\Omega + 2K$, the three levels are described by the 3×3 effective Hamiltonian,

$$\hat{H}_{\text{eff}} = \begin{pmatrix} \delta\omega^{(O)}(\vec{k}) & -g & 0 \\ -g & \delta\omega^{(M)}(\vec{k}) & \mathcal{K}(\vec{k}) \\ 0 & \mathcal{K}^*(\vec{k}) & \delta\omega^{(M)}(\vec{k}) \end{pmatrix},$$

where $\delta\omega^{(0)} = -\Delta - 4J - \Omega - 2K + 2Jk^2$, $\delta\omega^{(M)} = -Kk^2$, and $\mathcal{K} = K(k_x + ik_y)^2$. If $\delta\omega^{(0)}(k) > 0$, the optical bands do not cross the mechanical bands but push down the clockwise phonon mode, creating a band gap. For very small k (of the order of g/J), the bands might also form polaritons. As the detuning increases, the optical interaction becomes weaker and tends to close the gap. The minimal splitting is reached when the optically induced interaction is of the same order as the coupling $\mathcal{K}(k)$ between the mechanical modes with opposite quasiangular momentum. For $|\delta\omega^{(0)}(k) - \delta\omega^{(M)}(k)| \gg |\mathcal{K}(k)|, g$, we can eliminate adiabatically the low-frequency optical mode. The effective Hamiltonian for the remaining (mechanical) levels reads

$$\tilde{H}^{(\text{eff})} = \begin{pmatrix} \omega^{(M)}(\vec{k}) - \frac{g^2}{\omega^{(0)}(\vec{k})} & \mathcal{K}(\vec{k}) \\ \mathcal{K}^*(\vec{k}) & \omega^{(M)}(\vec{k}) \end{pmatrix}.$$

Thus, the eigenfrequencies of the second and third phononic bands are (in the original frame)

$$E_{2/3} = \Omega + 2K - Kk^2 - \frac{g^2}{2\omega^{(0)}(k)} \mp \sqrt{\frac{g^4}{4\omega^{(0)}(k)} + K^2k^4},$$

independent of the direction of the quasimomentum. The gap ω_{gap} between these two bands is given by the minimum of $E_3 - E_2$ over the quasimomentum k. For concreteness, we consider the case where the red sideband of the lowest frequency optical mode coincides with the largest frequency mechanical mode, $-\Delta - 4J = \Omega + 2K$. In this case, we find a simple expression for the minimal splitting, $\omega_{\text{gap}} \approx g\sqrt{2K/J}$.

In the most general case, we compute numerically the largest band gap as a function of the laser parameters. For fixed laser amplitude, the largest band gap size varies on a broad range as a function of the laser frequency; see Fig. 5. Notice that the mechanical eigenfrequency Ω is not specified in Fig. 5(a). It has been implicitly assumed to be the largest frequency in the problem while neglecting the Stokes scattering (which involves a rotating wave approximation), whence the band gaps become independent of Ω. Hence, the full phase diagram shown in Fig. 2 can be explored for an appropriately large value of Ω. On the other hand, the effect of Stokes scattering has to be carefully analyzed for large bandwidths $J/\Omega \gg 1$ or large couplings $g^2 \gg \Omega\kappa$. Below, we show that the interplay of dissipation and Stokes scattering restricts the laser parameter range where the system is stable. In particular, we focus on the experimentally most relevant regime of large optical bandwidth, $J \gg \Omega$, where a mechanical lasing transition arises.

APPENDIX F: CALCULATION OF THE DENSITY OF STATES AND TRANSMISSION PROBABILITIES FOR A FINITE SYSTEM

In Figs. 3 and 4, we show the LDOS on site l, $\rho_O(\omega, l)$ for photons and $\rho_M(\omega, l)$ for phonons, as well as the probabilities $T_{OO}(\omega, l, j)$ and $T_{MO}(\omega, l, j)$ that a photon (O for optical) injected on site j is transmitted to site l as a photon or a phonon (M for mechanical), respectively. They are directly related to the retarded Green function in frequency space, $\tilde{G}(\omega, l, j) = \int_{-\infty}^{\infty} dt e^{i\omega t} G(t, l, j)$, where the different interesting components are $G_{OO}(t,i,j) = -i\Theta(t)\langle[\hat{a}_i(t), \hat{a}_j^\dagger(0)]\rangle$ (propagation of a photon), $G_{MO}(t,i,j) = -i\Theta(t)\langle[\hat{b}_i(t), \hat{a}_j^\dagger(0)]\rangle$ (conversion of a photon to a phonon), and $G_{MM}(t, i, j) = -i\Theta(t)\langle[\hat{b}_i(t), \hat{b}_j^\dagger(0)]\rangle$ (propagation of a phonon)].

In order to calculate $\tilde{G}(\omega, l, j)$ numerically in a finite system with $N \times M$ unit cells (see Fig. 4), one organizes all the fields in a $12NM$-dimensional vector $\vec{\hat{c}}$ whose entries are $\hat{a}_j$, $\hat{a}_j^\dagger$, $\hat{b}_j$, $\hat{b}_j^\dagger$ for all possible $3NM$ lattice sites. Then,

Eq. (A3) can be written in a compact form as $i\dot{\vec{c}} = A\vec{c} + \vec{\xi}$ and the Green function is $\tilde{G}(\omega) = (\omega - A)^{-1}$. Notice that, in a system with $N \times M$ complete unit cells, the top and right edges have a zigzag form. In order to effectively describe a system with only straight edges, we set the hopping rates from and to the sites on the zigzag edges to zero. The photon and phonon LDOS are given by

$$\rho_O(\omega, l) = -2\mathrm{Im}\tilde{G}_{OO}(\omega, l, l),$$
$$\rho_M(\omega, l) = -2\mathrm{Im}\tilde{G}_{MM}(\omega, l, l),$$

respectively. Moreover, from the Kubo formula and the input-output relations $\hat{a}_j^{(\mathrm{out})} = \hat{a}_j^{(\mathrm{in})} - \sqrt{\kappa}\hat{a}_j$ (and likewise for the phononic fields), we find

$$T_{OO}(\omega, l, j) = |\delta_{lj} - i\kappa\tilde{G}_{OO}(\omega, l, j)|^2,$$
$$T_{MO}(\omega, l, j) = \kappa\gamma|\tilde{G}_{MO}(\omega, l, j)|^2,$$
$$T_{MM}(\omega, l, j) = \gamma^2|\tilde{G}_{MM}(\omega, l, j)|^2.$$

For a strip that is infinite in the longitudinal direction and of finite width M unit cells (see Fig. 3), the quasimomentum in the longitudinal direction is a conserved quantity. Hence, the LDOS is most conveniently calculated by taking a partial Fourier transform of the corresponding index n in Eq. (A3). For a numerical evaluation, one considers a finite length N and introduces periodic boundary conditions for n, $\hat{a}_j = N^{-1/2}\sum_n e^{ikn}\hat{a}_{kms}$ (and likewise for $\hat{b}_{kms}$). For N large enough, the finite size effects due to the finite length are smeared out by dissipation. For the strip, we organize the fields $\hat{a}_{kms}$, $\hat{a}^\dagger_{-kms}$, $\hat{b}_{kms}$, $\hat{b}^\dagger_{-kms}$ in a $12M$-dimensional vector $\vec{\hat{c}}_k$. Then, the Langevin equation reads $i\dot{\vec{\hat{c}}}_k = A_k\vec{\hat{c}}_k$ and the corresponding Green function is $\tilde{G}(\omega, k) = (\omega - A_k)^{-1}$. We arrive at the photon and phonon LDOS:

$$\rho_O(\omega, n, s) = -2N^{-1}\mathrm{Im}\sum_k \tilde{G}_{OO}(\omega, k; n, s; n, s),$$
$$\rho_M(\omega, n, s) = -2N^{-1}\mathrm{Im}\sum_k \tilde{G}_{MM}(\omega, k; n, s; n, s).$$

APPENDIX G: EDGE STATE TRANSPORT: ANALYSIS OF LOSS

In this appendix, we give more details regarding the photon and phonon transport in the optomechanical array. Our goal in this appendix is to analyze the propagation length of phonons in the chiral edge states. In addition, we discuss the appearance of a small but finite bulk density of states even inside the band gap. We argue that the directionality of the transport is maintained in spite of that effect.

We focus on the most promising and realistic parameter regime, where the optical bandwidth is much larger than the mechanical eigenfrequency (keeping the parameters of Fig. 3). In order to obtain the phonon propagation length, we consider injection at a particular site on the edge of a finite-size system (with a geometry similar to Fig. 4). In Fig. 6, we plot the decay of the phonon probability for different values of the intrinsic mechanical decay rate γ. These values are compatible with present-day experiments on optomechanical crystals, where even higher mechanical Q factors (10^5 and more) are reached routinely [38]. After some transient behavior close to the injection point (where photons are converted into phonons), the number of transmitted phonons decays exponentially with the propagation distance. This allows us to extract the propagation

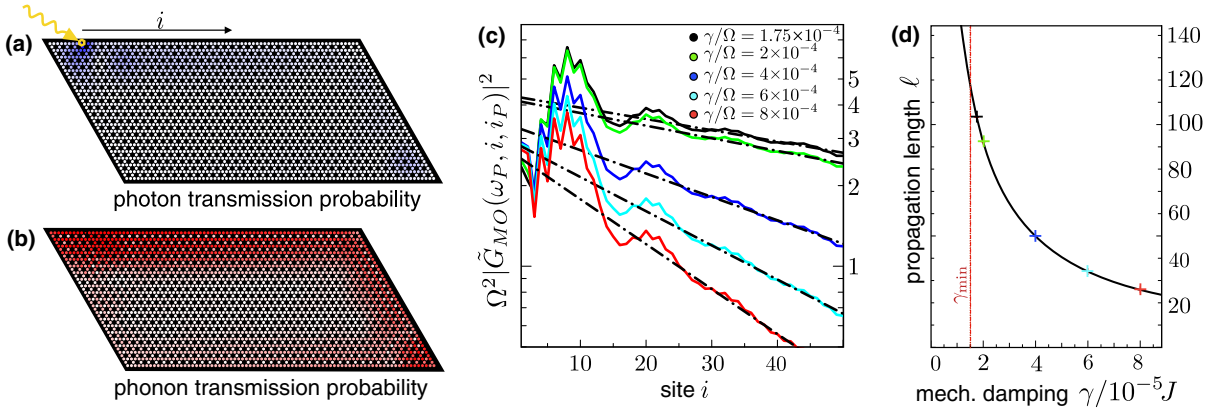

FIG. 6. Photon and phonon transport in the regime of large optical bandwidths. Panels (a) and (b) display the Green functions $|\tilde{G}_{OO}|^2$ and $|\tilde{G}_{MO}|^2$ for the propagation of photons and phonons, respectively, after injection of a probe laser photon at a frequency ω inside the gap. Panel (c) is a cut along the upper edge of (b), for several different values of the mechanical damping $\gamma/\Omega = 1.75\times10^{-4}$, $2\times10^{-4}, 4\times10^{-4}, 6\times10^{-4}, 8\times10^{-4}$ (from top to bottom), drawn on a log scale to visualize the exponential decay of phonon intensity. Panel (d) shows the propagation length ℓ directly obtained by a fit of the data from (c) (symbols) and by using the resulting data to fit the function $v/(\gamma + \gamma_O)$ with the optically induced damping γ_O as a fitting parameter (solid line). The mechanical decay rate in (a) and (b) is $\gamma = 4\times10^{-4}\ \Omega$. All other parameters are those of Fig. 3, on a 20×40 array, at $\omega/J = 0.10943$ (the middle of the band gap).

length ℓ [see panel (d)]. We expect ℓ to be given by the edge state speed divided by the overall mechanical decay rate $\gamma_{\text{total}} = \gamma + \gamma_O$ (the sum of the intrinsic and the optically induced mechanical decay rates). By extracting ℓ from a fit of the numerical data, we find that indeed $\ell = v/\gamma_{\text{total}}$, where the speed $v = 2\partial\omega(k)/\partial k$ (with two sites per unit cell along the edge) is obtained from the edge state dispersion in a strip geometry. The typical scale of ℓ is roughly given by the ratio of the phonon hopping K over the mechanical decay rate γ. This rule of thumb applies to the broad parameter range where the optically induced mechanical hopping and decay rates are, at most, of the order of their intrinsic counterpart. From our fits we can also extract the optically induced damping, which turns out to be comparatively small ($\gamma_O/\Omega = 4.2 \times 10^{-5}$). We note in passing that γ should be larger than a finite threshold to avoid the mechanical lasing instability analyzed in Appendix H; see Eq. (H2). For the regime discussed here, that would imply $\gamma > g^2\kappa/\Omega^2$, which we have ensured to be true in the figures. This sets an upper limit on ℓ that depends on the remaining parameters.

Next, we comment on the transient behavior close to the injection point; see Fig. 6. The initial transient behavior in the vicinity of the injection point [Fig. 6(c)] is partially due to photon-phonon conversion and the fact that we choose to inject locally (at a single site). We now discuss an additional effect during injection that is due to a residual contribution to the bulk DOS inside the band gap, which, though small, is noticeable; see also Fig. 3(g). We find that this is due to the broadening induced by mechanical dissipation. In particular, it results from the tail of the nearby large and narrow DOS peak formed by the localized excitations of the kagome flatband. The peak is so high that even a weak broadening can induce a non-negligible bulk DOS inside the band gap. A phonon injected locally will tunnel not only to the edge state but also (with a lower probability) to such localized excitations (after which it will decay without moving far). This is because local injection, in principle, can produce excitations at any quasimomentum k; i.e., it also covers the full range of k where the small dissipation-induced tail of the bulk band is present. Apart from this influence on the injection process, the small finite bulk DOS inside the gap can also have some influence during the propagation, if there is disorder that is not smooth on the scale of the unit cell. Then there can also be scattering with large momentum transfer that will be able to scatter some fraction of the edge state excitations into the dissipative tails of the localized bulk modes. We emphasize though that the directionality of the transport is preserved in any case (since phonons in the localized bulk modes no longer contribute to transport).

In addition, the injection losses could be reduced further by injecting excitations in a momentum-resolved way, over a small interval of momenta. Heisenberg's uncertainty relation then necessarily implies that they cannot be injected at a single point but rather over an extended region, e.g., by tunneling from a nearby phonon waveguide. In fact, to some extent, such a momentum-resolved injection even happens when exciting the system optically, since the largest photon-phonon coupling occurs in a limited range of quasimomenta (near $k = 0$ for this parameter regime).

As for Fig. 4, we note that in comparison to Fig. 3 we consider a smaller optical hopping J (by 1 order of magnitude) and a slightly larger optomechanical coupling g. This parameter choice allows us to display an edge state in a comparatively smaller array, since a smaller J implies shorter-range optically induced mechanical hopping and thus a smaller width of the edge states.

APPENDIX H: MECHANICAL LASING INSTABILITY

Here, we show that the optical backaction can cause a mechanical lasing instability for large enough couplings and optical bandwidths. There is a phonon lasing instability if at least one mechanical mode, at any point in the Brillouin zone, becomes unstable (negative damping rate). Initially, we analyze the damping rates at the symmetry point $\vec{\Gamma}$. There, it is convenient to write the OM interaction in terms of the eigenstates of the $\mathcal{C}_3$ rotations with quasimomentum $\vec{\Gamma}$: $\hat{b}_\oslash = (\mathcal{N})^{-1/2}\sum_l \hat{b}_l$, $\hat{b}_\circlearrowleft = (\mathcal{N})^{-1/2}\sum_l e^{i\varphi_l}\hat{b}_l$, $\hat{b}_\circlearrowright = (\mathcal{N})^{-1/2}\sum_l e^{-i\varphi_l}\hat{b}_l$, and likewise for $\hat{a}_\oslash$ $\hat{a}_\circlearrowleft$, and $\hat{a}_\circlearrowright$. Here and in the following, we omit the quasimomentum label $\vec{\Gamma}$, $\mathcal{N}$ is the overall number of sites forming the lattice, and the phases φ_l depend on only the site A, B, C within the unit cell. The linearized OM interaction reads

$$\frac{H_{\text{OM}}(\vec{\Gamma})}{\hbar} \approx -g[\hat{a}^\dagger_\circlearrowright \hat{b}_\circlearrowleft + \hat{a}^\dagger_\oslash \hat{b}^\dagger_\circlearrowleft] - g[\hat{a}^\dagger_\oslash \hat{b}_\circlearrowright + \hat{a}^\dagger_\circlearrowright \hat{b}^\dagger_\circlearrowright] - g[\hat{a}^\dagger_\circlearrowleft \hat{b}_\oslash + \hat{a}^\dagger_\circlearrowleft \hat{b}^\dagger_\oslash] + \text{H.c.}$$

As it should be expected from quasi-angular-momentum conservation, when a driving photon (which carries a vortex) emits a phonon with a vortex $|\circlearrowleft, M\rangle$, it is simultaneously converted into a vortex-free array photon (in the optical mode $|\oslash, O\rangle$, with eigenfrequency $\omega_{\text{phot}} - 4J$), whereas when it absorbs a phonon from the same mechanical mode, it is converted into an array photon with an antivortex (in the optical mode $|\circlearrowright, O\rangle$, with eigenfrequency $\omega_{\text{phot}} + 2J$). This is a peculiar situation, with different photon creation processes connected to phonon absorption and emission, respectively. It can take place only because the time-reversal symmetry is broken. Since the coupling strength of both processes is the same (namely, $-g$), we have antidamping of the mechanical mode $|\circlearrowleft, M\rangle$ if the blue sideband frequency $\omega_L - \Omega$ is closer to the eigenfrequency of $|\oslash, O\rangle$ than the red sideband frequency $\omega_L + \Omega$ is to the eigenfrequency of $|\circlearrowright, O\rangle$. In the opposite situation, we have damping.

There are two possible scenarios: The first scenario occurs for large bandwidths, $J > \Omega/3$. Then, the blue sideband of the optical mode $|\oslash, O\rangle$, located at $\omega_{\rm phot} - 4J + \Omega$, has lower frequency than the red sideband of $|\circlearrowright, O\rangle$, located at $\omega_{\rm phot} - 4J + \Omega$. In this case, the optical backaction tends to amplify the mechanical mode $|\circlearrowleft, M\rangle$ when the driving is red detuned (its frequency is below the average eigenfrequency of the two optical modes, $-\Delta - J > 0$). Instead, the mechanical mode is damped by the optical backaction for a blue detuned drive ($-\Delta - J < 0$). This behavior is completely opposite to the standard scenario in optomechanics. A similar analysis shows that the mechanical mode $|\circlearrowright, M\rangle$ shows the opposite behavior. Hence, for *any* choice of laser frequency, either $|\circlearrowleft, M\rangle$ or $|\circlearrowright, M\rangle$ is antidamped (provided $J > \Omega/3$). The optically induced antidamping grows with increasing coupling and eventually overcomes the intrinsic damping, thus generating a mechanical lasing transition at a critical coupling.

The second scenario occurs for small bandwidths, $J < \Omega/3$. Then, the blue sideband near $|\oslash, O\rangle$ has a higher frequency than the red sideband of $|\circlearrowright, O\rangle$. In this case, the optical backaction damps the mechanical mode $|\circlearrowleft, M\rangle$ for a red-detuned laser ($-\Delta - J > 0$) and amplifies it for a blue-detuned drive ($-\Delta - J < 0$). That is the standard behavior in optomechanical systems. A similar analysis shows that the mechanical mode $|\circlearrowright, M\rangle$ displays the same behavior. Since, at $\vec{\Gamma}$ the spacing between the optical eigenstates is largest, the same conclusion can be drawn for any momentum. We can conclude that in the small bandwidth case, $J < \Omega/3$, there is a mechanical lasing transition for a blue-detuned drive but not for a red-detuned drive. Notice that the region where no unwanted mechanical lasing transition is present for small bandwidth J includes the central part of the phase diagram Fig. 2 (where a number of different topological phases appear), as well as the "tight-binding limit" region on the right-hand part of the diagram.

It is possible to analytically compute the threshold of the mechanical lasing transition for large bandwidths $J \gg \Omega$ and when the driving frequency is below the blue sideband of the lowest frequency optical mode $|\oslash, O\rangle$ (at the $\vec{\Gamma}$ point), $-\Delta - 4J > -\Omega - 2K$. Since the other blue sidebands have larger detuning, the lasing transition is determined by the backaction of $|\oslash, O\rangle$ on the mechanical mode $|\circlearrowleft, M\rangle$. In order to get simple formulas, we neglect the backaction by the optical modes $|\circlearrowright, O\rangle$ and $|\circlearrowleft, O\rangle$. This is a good approximation as these modes are far detuned for a large optical bandwidth. The Langevin equations for the modes $\hat{a}_{\oslash}$, $\hat{b}_{\circlearrowright}$, and $\hat{b}_{\circlearrowleft}$ read

$$\begin{aligned}
\dot{\hat{a}}_{\oslash} &= (i\Delta + i4J - \kappa/2)\hat{a}_{\oslash} + ig(\hat{b}_{\circlearrowright} + b^{\dagger}_{\circlearrowleft}) + \sqrt{\kappa}\hat{a}^{(\rm in)}_{\oslash},\\
\dot{\hat{b}}_{\circlearrowright} &= (-i\Omega - i2K - \gamma/2)\hat{b}_{\circlearrowright} + ig\hat{a}_{\oslash} + \sqrt{\gamma}\hat{b}^{(\rm in)}_{\circlearrowright},\\
\dot{\hat{b}}_{\circlearrowleft} &= (-i\Omega - i2K - \gamma/2)\hat{b}_{\circlearrowleft} + ig\hat{a}^{\dagger}_{\oslash} + \sqrt{\gamma}\hat{b}^{(\rm in)}_{\circlearrowleft}.
\end{aligned}$$

As before, we divide $\hat{a}_{\oslash}$ into its blue and red sidebands as well as its intrinsic quantum fluctuations (optical vacuum noise):

$$\hat{a}_{\oslash} \equiv e^{-i\Omega t}\hat{a}^{(\rm red)} + e^{i\Omega t}\hat{a}^{(\rm blue)} + \delta\hat{a}.$$

For a narrow mechanical bandwidth $\gamma \ll \Omega$, the operators $\hat{a}^{(\rm red)}$ and $\hat{a}^{(\rm blue)}$ are slowly varying and we can neglect their derivative in the first Langevin equation. Then, we find

$$\begin{aligned}
\hat{a}_{\oslash} = &\frac{ig}{\kappa/2 - i(\Delta + 4J + \Omega + 2K)}\hat{b}_{\circlearrowright}\\
&+ \frac{ig}{\kappa/2 - i(\Delta + 4J - \Omega - 2K)}\hat{b}^{\dagger}_{\circlearrowleft} + \delta\hat{a},
\end{aligned}$$

where $\delta\hat{a}$ describes the vacuum noise. By substituting in the second and third Langevin equations and performing a rotating wave approximation, we find

$$\begin{aligned}
\dot{\hat{b}}_{\circlearrowright} &= (-i\Omega^{(\rm eff)}_{\circlearrowright} - \gamma^{(\rm eff)}_{\circlearrowright}/2)\hat{b}_{\circlearrowright} + \hat{\eta}_{\circlearrowright},\\
\dot{\hat{b}}_{\circlearrowleft} &= (-i\Omega^{(\rm eff)}_{\circlearrowleft} - \gamma^{(\rm eff)}_{\circlearrowleft}/2)\hat{b}_{\circlearrowleft} + \hat{\eta}_{\circlearrowleft}.
\end{aligned}$$

Here, $\hat{\eta}_{\circlearrowright/\circlearrowleft}$ contains the intrinsic mechanical as well as the optically induced noise. The effective eigenfrequencies $\Omega^{(\rm eff)}_{\circlearrowright/\circlearrowleft}$ and decay rates $\gamma^{(\rm eff)}_{\circlearrowright/\circlearrowleft}$ are obtained as

$$\begin{aligned}
\Omega^{(\rm eff)}_{\circlearrowright} &= \Omega + 2K + \frac{g^2(\Delta + 4J + \Omega + 2K)}{(\kappa/2)^2 + (\Delta + 4J + \Omega + 2K)^2},\\
\gamma^{(\rm eff)}_{\circlearrowright} &= \gamma + \frac{g^2\kappa}{(\kappa/2)^2 + (\Delta + 4J + \Omega + 2K)^2},\\
\Omega^{(\rm eff)}_{\circlearrowleft} &= \Omega + 2K + \frac{g^2(\Delta + 4J - \Omega - 2K)}{(\kappa/2)^2 + (\Delta + 4J - \Omega - 2K)^2},\\
\gamma^{(\rm eff)}_{\circlearrowleft} &= \gamma - \frac{g^2\kappa}{(\kappa/2)^2 + (\Delta + 4J - \Omega - 2K)^2}.
\end{aligned} \tag{H1}$$

We reach the threshold of the mechanical lasing transition when the smaller rate reaches zero, $\gamma^{(\rm eff)}_{\circlearrowright} = 0$, corresponding to a maximum tolerable cooperativity (before hitting the instability) of

$$\mathcal{C} = 4\frac{g^2}{\kappa\gamma} = 1 + \left(\frac{\Delta + 4J - \Omega - 2K}{\kappa/2}\right)^2. \tag{H2}$$

Our formula holds for a laser driving frequency below the blue sideband of the lowest frequency optical mode $|\oslash, O\rangle$, $-\Delta - 4J > -\Omega - 2K$. The threshold cooperativity increases monotonically from $\mathcal{C} = 1$ to infinity for decreasing laser frequency. Notice that $\mathcal{C} = 1$ also represents the lower bound for the maximum tolerable cooperativity. It is reached when the driving is close to the blue sideband of any optical mode.

APPENDIX I: STABILITY DIAGRAM

In the general case, each relaxation process towards the classical solution Eq. (A2) is associated with a pole of the Green function $\tilde{G}(\omega, l, j)$ lying in the lower-half complex plane. The corresponding damping rate is given by twice the distance of the pole from the real axis. A pole in the upper-half plane is associated with an excitation with negative damping and signals that solution Eq. (A2) is unstable. In Fig. 5, we plot the damping rate of the slowest relaxation process as a function of the laser parameters for $J = \Omega$. The unstable region where the Green function $\tilde{G}(\omega, l, j)$ has at least one pole in the upper-half plane is marked in black. The analytical expression for the border of the mechanical lasing instability Eq. (H2) is plotted in yellow. It is derived for laser frequencies below the blue sideband of the lowest frequency optical mode (the right-hand side of the stability diagram). In the central part of the diagram corresponding to the strong-coupling regime, the maximum tolerable cooperativity stays close to its lower bound $\mathcal{C} = 1$ because the driving frequency is always close to the blue sideband of an optical state. In the left-hand part of the diagram, the driving frequency is larger than the blue sideband of the largest frequency mode and the lasing thresold starts to increase again. Notice that at the far right of the diagram the solution become unstable for values of the cooperativity below the threshold of the mechanical lasing instability Eq. (H2). In this regime, the instability is not induced by mechanical lasing but by a parametric instability. In optomechanical arrays, parametric instabilities can occur for $g^2 \gtrsim \Omega\kappa$ [39,49]. They set a finite limit to the tolerable cooperativity also in systems with a small bandwidth driven by a red-detuned laser where no mechanical lasing transition is present.

[1] M. Z. Hasan and C. L. Kane, *Colloquium: Topological Insulators*, Rev. Mod. Phys. **82**, 3045 (2010).

[2] D. J. Thouless, M. Kohmoto, M. P. Nightingale, and M. den Nijs, *Quantized Hall Conductance in a Two-Dimensional Periodic Potential*, Phys. Rev. Lett. **49**, 405 (1982).

[3] F. D. M. Haldane, *Model for a Quantum Hall Effect without Landau Levels: Condensed-Matter Realization of the "Parity Anomaly,"* Phys. Rev. Lett. **61**, 2015 (1988).

[4] C. L. Kane and E. J. Mele, *Z2 Topological Order and the Quantum Spin Hall Effect*, Phys. Rev. Lett. **95**, 146802 (2005).

[5] B. Andrei Bernevig and S.-C. Zhang, *Quantum Spin Hall Effect*, Phys. Rev. Lett. **96**, 106802 (2006).

[6] T. Oka and H. Aoki, *Photovoltaic Hall Effect in Graphene*, Phys. Rev. B **79**, 081406 (2009).

[7] Z. Gu, H. A. Fertig, D. P. Arovas, and A. Auerbach, *Floquet Spectrum and Transport through an Irradiated Graphene Ribbon*, Phys. Rev. Lett. **107**, 216601 (2011).

[8] N. H. Lindner, G. Refael, and V. Galitski, *Floquet Topological Insulator in Semiconductor Quantum Wells*, Nat. Phys. **7**, 490 (2011).

[9] T. Kitagawa, M. A. Broome, A. Fedrizzi, M. S. Rudner, E. Berg, I. Kassal, A. Aspuru-Guzik, E. Demler, and A. G. White, *Observation of Topologically Protected Bound States in Photonic Quantum Walks*, Nat. Commun. **3**, 882 (2012).

[10] A. Bermudez, T. Schaetz, and D. Porras, *Photon-Assisted-Tunneling Toolbox for Quantum Simulations in Ion Traps*, New J. Phys. **14**, 053049 (2012).

[11] N. Goldman, G. Juzeliūnas, P. Öhberg, and I. B. Spielman, *Light-Induced Gauge Fields for Ultracold Atoms*, Rep. Prog. Phys. **77**, 126401 (2014).

[12] M. Atala, M. Aidelsburger, J. T. Barreiro, D. Abanin, T. Kitagawa, E. Demler, and I. Bloch, *Direct Measurement of the Zak Phase in Topological Bloch Bands*, Nat. Phys. **9**, 795 (2013).

[13] L. Duca, T. Li, M. Reitter, I. Bloch, M. Schleier-Smith, and U. Schneider, *An Aharonov-Bohm Interferometer for Determining Bloch Band Topology*, Science **347**, 288 (2015).

[14] G. Jotzu, M. Messer, R. Desbuquois, M. Lebrat, T. Uehlinger, D. Greif, and T. Esslinger, *Experimental Realization of the Topological Haldane Model with Ultracold Fermions*, Nature (London) **515**, 237 (2014).

[15] F. D. M. Haldane and S. Raghu, *Possible Realization of Directional Optical Waveguides in Photonic Crystals with Broken Time-Reversal Symmetry*, Phys. Rev. Lett. **100**, 013904 (2008).

[16] J. Koch, A. A. Houck, K. Le Hur, and S. M. Girvin, *Time-Reversal-Symmetry Breaking in Circuit-QED-Based Photon Lattices*, Phys. Rev. A **82**, 043811 (2010).

[17] M. Hafezi, E. A. Demler, M. D. Lukin, and J. M. Taylor, *Robust Optical Delay Lines with Topological Protection*, Nat. Phys. **7**, 907 (2011).

[18] R. O. Umucalılar and I. Carusotto, *Artificial Gauge Field for Photons in Coupled Cavity Arrays*, Phys. Rev. A **84**, 043804 (2011).

[19] K. Fang, Z. Yu, and S. Fan, *Realizing Effective Magnetic Field for Photons by Controlling the Phase of Dynamic Modulation*, Nat. Photonics **6**, 782 (2012).

[20] M. Hafezi and P. Rabl, *Optomechanically Induced Non-Reciprocity in Microring Resonators*, Opt. Express **20**, 7672 (2012).

[21] A. B. Khanikaev, S. Hossein Mousavi, W.-K. Tse, M. Kargarian, A. H. MacDonald, and G. Shvets, *Photonic Topological Insulators*, Nat. Mater. **12**, 233 (2012).

[22] Z. Wang, Y. Chong, J. D. Joannopoulos, and M. Soljacic, *Observation of Unidirectional Backscattering-Immune Topological Electromagnetic States*, Nature (London) **461**, 772 (2009).

[23] M. Hafezi, S. Mittal, J. Fan, A. Migdall, and J. M. Taylor, *Imaging Topological Edge States in Silicon Photonics*, Nat. Photonics **7**, 1001 (2013).

[24] M. C. Rechtsman, J. M. Zeuner, Y. Plotnik, Y. Lumer, D. Podolsky, F. Dreisow, S. Nolte, M. Segev, and A. Szameit, *Photonic Floquet Topological Insulators*, Nature (London) **496**, 196 (2013).

[25] L. D. Tzuang, K. Fang, P. Nussenzveig, S. Fan, and M. Lipson, *Non-Reciprocal Phase Shift Induced by an Effective Magnetic Flux for Light*, Nat. Photonics **8**, 701 (2014).

[26] L. Lu, J. D. Joannopoulos, and M. Soljacic, *Topological Photonics*, Nat. Photonics **8**, 821 (2014).

[27] E. Prodan and C. Prodan, *Topological Phonon Modes and Their Role in Dynamic Instability of Microtubules*, Phys. Rev. Lett. **103**, 248101 (2009).

[28] C. L. Kane and T. C. Lubensky, *Topological Boundary Modes in Isostatic Lattices*, Nat. Phys. **10**, 39 (2014).

[29] B. Gin-ge Chen, N. Upadhyaya, and V. Vitelli, *Nonlinear Conduction via Solitons in a Topological Mechanical Insulator*, Proc. Natl. Acad. Sci. U.S.A. **111**, 13004 (2014).

[30] J. Paulose, B. Gin-ge Chen, and V. Vitelli, *Topological Modes Bound to Dislocations in Mechanical Metamaterials*, Nat. Phys. **11**, 153 (2015).

[31] Z. Yang, F. Gao, X. Shi, X. Lin, Z. Gao, Y. Chong, and B. Zhang, *Topological Acoustics*, Phys. Rev. Lett. **114**, 114301 (2015).

[32] R. Süsstrunk and S. D. Huber, *Observation of Phononic Helical Edge States in a Mechanical Topological Insulator*, Science **349**, 47 (2015).

[33] M. Aspelmeyer, T. J. Kippenberg, and F. Marquardt, *Cavity Optomechanics*, Rev. Mod. Phys. **86**, 1391 (2014).

[34] M. Eichenfield, J. Chan, R. M. Camacho, K. J. Vahala, and O. Painter, *Optomechanical Crystals*, Nature (London) **462**, 78 (2009).

[35] A. H. Safavi-Naeini, T. P. Mayer Alegre, M. Winger, and O. Painter, *Optomechanics in an Ultrahigh-Q Two-Dimensional Photonic Crystal Cavity*, Appl. Phys. Lett. **97**, 181106 (2010).

[36] E. Gavartin, R. Braive, I. Sagnes, O. Arcizet, A. Beveratos, T. J. Kippenberg, and I. Robert-Philip, *Optomechanical Coupling in a Two-Dimensional Photonic Crystal Defect Cavity*, Phys. Rev. Lett. **106**, 203902 (2011).

[37] J. Chan, T. P. Mayer Alegre, A. H. Safavi-Naeini, J. T. Hill, A. Krause, S. Groblacher, M. Aspelmeyer, and O. Painter, *Laser Cooling of a Nanomechanical Oscillator into Its Quantum Ground State*, Nature (London) **478**, 89 (2011).

[38] A. H. Safavi-Naeini, J. T. Hill, S. Meenehan, J. Chan, S. Gröblacher, and O. Painter, *Two-Dimensional Phononic-Photonic Band Gap Optomechanical Crystal Cavity*, Phys. Rev. Lett. **112**, 153603 (2014).

[39] M. Schmidt, V. Peano, and F. Marquardt, *Optomechanical Dirac physics*, New J. Phys. **17**, 023025 (2015).M. Schmidt, S. Kessler, V. Peano, and F. Marquardt, *Optomechanical creation of magnetic fields for photons on a lattice* , Optica **2**, 635 (2015).

[40] T. Karzig, C.-E. Bardyn, N. H. Lindner, and G. Refael, *Topological Polaritons from Quantum Wells in Photonic Waveguides or Microcavities*, Phys. Rev. X **5**, 031001 (2015).

[41] A. V. Nalitov, D. D. Solnyshkov, and G. Malpuech, *Polariton $\mathbb{Z}$ Topological Insulator*, Phys. Rev. Lett. **114**, 116401 (2015).

[42] C.-E. Bardyn, T. Karzig, G. Refael, and T. C. H. Liew, *Topological Polaritons and Excitons in Garden-Variety Systems*, Phys. Rev. B **91**, 161413 (2015).

[43] G. Heinrich, M. Ludwig, J. Qian, B. Kubala, and F. Marquardt, *Collective Dynamics in Optomechanical Arrays*, Phys. Rev. Lett. **107**, 043603 (2011).

[44] D. E. Chang, A. H. Safavi-Naeini, M. Hafezi, and O. Painter, *Slowing and Stopping Light Using an Optomechanical Crystal Array*, New J. Phys. **13**, 023003 (2011).

[45] A. Xuereb, C. Genes, and A. Dantan, *Strong Coupling and Long-Range Collective Interactions in Optomechanical Arrays*, Phys. Rev. Lett. **109**, 223601 (2012).

[46] M. Ludwig and F. Marquardt, *Quantum Many-Body Dynamics in Optomechanical Arrays*, Phys. Rev. Lett. **111**, 073603 (2013).

[47] A. H. Safavi-Naeini and O. Painter, *Proposal for an Optomechanical Traveling Wave Phonon-Photon Translator*, New J. Phys. **13**, 013017 (2011).

[48] M. Notomi, E. Kuramochi, and T. Tanabe, *Large-Scale Arrays of Ultrahigh-Q Coupled Nanocavities*, Nat. Photonics **2**, 741 (2008).

[49] W. Chen and A. A. Clerk, *Photon Propagation in a One-Dimensional Optomechanical Lattice*, Phys. Rev. A **89**, 033854 (2014).

[50] M. Schmidt, M. Ludwig, and F. Marquardt, *Optomechanical Circuits for Nanomechanical Continuous Variable Quantum State Processing*, New J. Phys. **14**, 125005 (2012).

[51] S. J. M. Habraken, K. Stannigel, M. D. Lukin, P. Zoller, and P. Rabl, *Continuous Mode Cooling and Phonon Routers for Phononic Quantum Networks*, New J. Phys. **14**, 115004 (2012).

[52] K. Ohgushi, S. Murakami, and N. Nagaosa, *Spin Anisotropy and Quantum Hall Effect in the Kagome Lattice: Chiral Spin State Based on a Ferromagnet*, Phys. Rev. B **62**, R6065 (2000).

[53] D. Green, L. Santos, and C. Chamon, *Isolated Flat Bands and Spin-1 Conical Bands in Two-Dimensional Lattices*, Phys. Rev. B **82**, 075104 (2010).

[54] H. Katsura, N. Nagaosa, and P. A. Lee, *Theory of the Thermal Hall Effect in Quantum Magnets*, Phys. Rev. Lett. **104**, 066403 (2010).

[55] A. H. Safavi-Naeini and O. Painter, *Design of Optomechanical Cavities and Waveguides on a Simultaneous Bandgap Phononic-Photonic Crystal Slab*, Opt. Express **18**, 14926 (2010).

[56] G. S. Agarwal and S. Huang, *Electromagnetically Induced Transparency in Mechanical Effects of Light*, Phys. Rev. A **81**, 041803 (2010).

[57] S. Weis, R. Rivière, S. Deléglise, E. Gavartin, O. Arcizet, A. Schliesser, and T. J. Kippenberg, *Optomechanically Induced Transparency*, Science **330**, 1520 (2010).

[58] A. H. Safavi-Naeini, T. P. Mayer Alegre, J. Chan, M. Eichenfield, M. Winger, Q. Lin, J. T. Hill, D. Chang, and O. Painter, *Electromagnetically Induced Transparency and Slow Light with Optomechanics*, Nature (London) **472**, 69 (2011).

[59] C. J. Chen, J. Zheng, T. Gu, J. F. McMillan, M. Yu, G.-Q. Lo, D.-L. Kwong, and C. W. Wong, *Selective Tuning of High-Q Silicon Photonic Crystal Nanocavities via Laser-Assisted Local Oxidation*, Opt. Express **19**, 12480 (2011).

[60] K. Schwab, E. A. Henriksen, J. M. Worlock, and M. L. Roukes, *Measurement of the quantum of thermal conductance*, Nature (London) **404**, 974 (2000).

[61] M. Kohomoto, *Topological Invariant and the Quantization of the Hall Conductance*, Ann. Phys. (N.Y.) **160**, 343 (1985).